

**DISSERTATION**

**DEVELOPMENT, CHARACTERIZATION AND APPLICATION OF**

**A HIGH AVERAGE POWER CAPILLARY DISCHARGE SOFT**

**X-RAY LASER**

Submitted by  
Brady Robert Benware  
Electrical and Computer Engineering Department

In partial fulfillment of the requirements  
For the degree of Doctor of Philosophy  
Colorado State University  
Fort Collins, Colorado  
Fall 2001

**COLORADO STATE UNIVERSITY**

October 25, 2001

WE HEREBY RECOMEND THAT THE DISSERTATION PREPARED UNDER OUR SUPERVISION BY BRADY ROBERT BENWARE ENTITLED DEVELOPMENT, CHARACTERIZATION AND APPLICATION OF A HIGH AVERAGE POWER CAPILLARY DISCHARGE SOFT X-RAY LASER BE ACCEPTED AS FULFILLING IN PART REQUIREMENTS FOR THE DEGREE OF DOCTOR OF PHILOSOPHY.

Committee on Graduate Work

*Sanjay*  
\_\_\_\_\_  
*Paul J. Willow*  
\_\_\_\_\_  
*George Rocca*  
\_\_\_\_\_  
Adviser  
\_\_\_\_\_  
Department Head *Sanjay*  
\_\_\_\_\_

**ABSTRACT OF DISSERTATION**

**DEVELOPMENT, CHARACTERIZATION AND APPLICATION OF**

**A HIGH AVERAGE POWER CAPILLARY DISCHARGE SOFT**

**X-RAY LASER**

A compact high repetition rate, high average power capillary discharge laser operating at a wavelength of 46.9 nm that is of the size of many widely utilized visible and UV lasers has been developed and characterized. Two significant differences from previously developed capillary discharge soft x-rays lasers, the use of ceramic capillaries rather than poly-acetal and significantly longer plasma columns of up to 36 cm, allowed for the generation of greatly increased output pulse energies and average power. Lasing at a repetition rate of 4 Hz and an average laser pulse energy of 0.88 mJ has been obtained, which amounts to an average power of 3.5 mW. Lasing at repetition rates as high as 10 Hz was also achieved, but with lower output pulse energy. In this work the beam energy and divergence were measured as a function of capillary length, and the temporal evolution of the laser pulse was also studied. The combined high pulse energy and high repetition rate of this laser make it unique in the field of soft x-ray lasers to date.

This laser has been used to perform angular dependent reflectivity measurements to determine optical constants of materials at 46.9 nm, which are in good agreement with

those previously measured, or in some cases represent the first recorded values at this wavelength. This experiment constitutes the first application of a table-top soft x-ray laser to the field of material characterization. In a separate experiment, the output beam was polarized using two multi-layer coated mirrors that were configured for optimum reflectivity at 45 degrees. The resulting 96% polarized beam was then used to characterize the efficiency of a diffraction grating. Finally, in a third experiment, the beam was focused using a spherical multi-layer coated mirror to a spot size where the majority of the energy was confined to a 2  $\mu\text{m}$  diameter. The peak intensity was estimated to be  $1 \times 10^{11} \text{ W/cm}^2$ . Through ray tracing computations, the focused spot size was determined to be dominated by spherical aberration. This focused beam reached intensities that were sufficient to induce ablation on brass and stainless steel targets realizing the first demonstration of material ablation with a coherent soft x-ray beam.

Brady Robert Benware  
Electrical and Computer Engineering Department  
Colorado State University  
Fort Collins, CO 80523  
Fall 2001

## TABLE OF CONTENTS

CHAPTER 1 .....	1
-----------------	---

### INTRODUCTION

1.1. Synopsis .....	1
1.2. Applications for table-top soft x-ray lasers .....	2
1.3. Current approaches to table-top soft x-ray lasers.....	4
1.4. Capillary discharge approach to SXRLs .....	9
1.5. Previous work.....	10
1.6. Alternatives to SXRLs for the generation of coherent soft x-ray radiation ..	13
1.7. Figures.....	16
1.8. References .....	19

CHAPTER 2 .....	22
-----------------	----

### HIGH AVERAGE POWER, HIGH REPETITION RATE TABLE TOP SOFT X-RAY LASER OPERATION AT 46.9 nm

2.1. Introduction .....	22
2.2. Development of the high average power table-top SXRL .....	23
2.3. Measurement of laser pulse energy.....	24
2.4. Operation in a highly saturated regime .....	26
2.5. Measurement of the far-field beam profile .....	28

2.6. Comparison of coherent laser output power to a synchrotron beamline.....	28
2.7. Conclusion.....	29
2.8. Figures.....	31
2.9. References.....	38

**CHAPTER 3..... 40**

**DETERMINATION OF XUV OPTICAL CONSTANTS BY  
REFLECTOMETRY USING A HIGH REPETITION RATE 46.9 nm  
LASER**

3.1. Introduction.....	40
3.2. Experimental Setup.....	42
3.3. Data analysis.....	44
3.4. Results of the determination of optical constants.....	47
3.5. Conclusion.....	52
3.6. Figures.....	54
3.7. References.....	62

**CHAPTER 4..... 64**

**GENERATION AND APPLICATION OF A HIGH AVERAGE POWER  
POLARIZED SOFT X-RAY LASER BEAM**

4.1. Introduction.....	64
4.2. Design and fabrication of polarizing mirrors.....	66
4.3. Generation of a polarized soft x-ray laser beam.....	67
4.4. Characterization of diffraction gratings.....	71

4.5. Conclusion.....	73
4.6. Figures.....	74
4.7. References .....	89
CHAPTER 5.....	81
FOCUSING OF A TABLE-TOP SOFT X-RAY LASER BEAM AND LASER ABLATION	
5.1. Introduction .....	81
5.2. Experimental setup.....	82
5.3. Results .....	83
5.4. Ray tracing computations.....	84
5.5. Conclusion.....	85
5.6. Figures.....	87
5.7. References .....	91
CHAPTER 6.....	92
SUMMARY	

# CHAPTER 1

## INTRODUCTION

### 1.1. Synopsis

The goal of the work of this dissertation was to demonstrate and characterize a table-top soft x-ray laser (SXRL) that could be used as a practical research tool, and to demonstrate its feasibility as such by performing several experiments. The laser developed in this work is an innovation on previous capillary discharge table-top soft x-ray lasers developed at Colorado State University [1.1,1.2,1.3] and is the first high average power soft x-ray laser demonstrated. This new generation capillary discharge laser has the important difference of using ceramic capillaries rather than the traditional polyacetal capillary and extended the capillary length to up to 36 cm. These changes allow the new device to produce more than 30 times the energy per pulse, run at more than 200 times the repetition rate and produce more than 4 orders of magnitude more average power than previous work[1.2].

In order to place this work in proper context, the remaining section of the first chapter of this dissertation will focus on the field of table-top soft x-ray lasers. A discussion of the current state of the field is followed by the specific evolution and previous work done on capillary discharge soft x-ray lasers developed at Colorado State

University. Chapter two details the improved discharge laser developed in this work and presents the results of the characterization of the beam pulse energy, spatial distribution and temporal distribution. Chapters three through five present the results of three independent experiments that represent the first application of a table-top soft x-ray laser to the fields of materials characterization and laser ablation.

## **1.2. Applications for table-top soft x-ray lasers**

Coherent soft x-ray radiation has important applications in numerous scientific disciplines. Coherent radiation at short wavelengths will be increasingly beneficial to fields such as spectroscopy, biology, plasma diagnostics, microscopy, radiography, chemistry, holography and lithography [1.4,1.5,1.6]. Some proof-of-principle demonstrations of soft x-ray lasers have already been achieved in microscopy [1.7,1.8], holography [1.9], diagnostics of dense plasmas [1.10, 1.11] and the excitation of nonlinear photoluminescence crystals [1.12].

An example of the potential benefit obtained by the use of soft x-ray radiation is the application to photoelectron micro-spectroscopy. This technique can provide information on element distributions and electronic structure of solid surfaces, clusters, and atoms with minimal damage to the samples. This application is ideally suited for soft x-ray sources because photons of just 100 eV (~12 nm) can excite inner shells of most elements with a few exceptions while lower energy photons would be more effective for excitation of valence band electrons [1.13]. Requirements of the light source for x-ray photoelectron micro-spectroscopy are that it has a high brilliance and a narrow linewidth for higher resolution [1.13]. Because of these requirements, compact soft x-ray lasers are quite attractive for this application.

High density plasma diagnostics is another example where these short wavelength lasers are becoming essential. The maximum electron density for which photons can propagate in a plasma is the critical density and is given by  $n_{cr}=1.1 \times 10^{21} \lambda^{-2}$  [ $\text{cm}^{-3}$ ] ( $\lambda$  in  $\mu\text{m}$ ). This is the density at which the index of refraction  $\eta=(1-n_e/n_{cr})^{1/2}$  is zero, and photons are attenuated and/or reflected. Thus, for shorter wavelengths, this critical density is higher and one can probe denser plasmas. In addition to the wavelength requirement, soft x-ray lasers could provide the coherence required to use plasma diagnostic techniques involving interferometry. Da Silva *et al.* have recently made measurements of the electron density in a laser produced plasma using a Mach-Zehnder interferometer and a 15.5 nm laser, pumped by the large NOVA laser [1.14]. They were able to probe plasmas with peak electron densities of  $4 \times 10^{21} \text{ cm}^{-3}$  for plasma lengths up to 3 mm. Work conducted at Colorado State University extended this work using a compact table-top discharge soft x-ray laser [1.15, 1.16].

Within this work, applications to material characterization and laser ablation have been demonstrated. Both of these fields can benefit from soft x-ray lasers as well. The laser in this work is an excellent source for the high pulse energies that are necessary for laser ablation while the narrow linewidth is important in the characterization of materials. In the future, this author believes that the applications will be widespread and numerous as sources for coherent soft x-ray radiation become widely available and more practical. As it has been in the history of the laser itself, the source has often predated the applications for it.

### 1.3. Current approaches to table-top soft x-ray lasers

The first soft x-ray lasers were demonstrated in the mid 1980's by groups from Lawrence Livermore National Labs and Princeton University. Both lasers were generated from laser created plasmas using very large pump lasers. For example, using the NOVA laser which was the world's largest laser to generate a plasma from a thin foil target, Matthews *et al.* at LLNL first demonstrated amplification in Ne-like Se at a wavelength of 20.6 nm and 21.0 nm [1.17]. In this case, the plasma has sufficient density and electron temperature to create ions in the Ne-like state and subsequently populate the laser upper level from the ionic ground state through electron impact excitation. At the same time, Suckewer *et al.* at Princeton University reported strong amplification at 18.2nm in a  $C_{VI}$  laser created plasma from a solid target [1.18]. Both results were ground breaking for the field of soft x-ray lasers and opened the door for important innovations to the fundamental concepts demonstrated by them. Aside from the obvious relentless pursuit of shorter wavelength lasers, there has been a great deal of interest in developing soft x-ray lasers that are of a more practical size, a so-called table-top soft x-ray source.

The low reflectivity of materials in the soft x-ray wavelength region coupled with the short gain lifetime associated with most x-ray laser schemes dictates that soft x-ray lasers operate without the use of an optical cavity or with only a half cavity. Lasing in this mode arises from strongly amplified spontaneous emission (ASE). Due to this, the gain length product of the plasma column generally judges the performance of soft x-ray lasers. A gain length product of  $gl > 5$  is often considered to be the benchmark for a clear demonstration of lasing within the SXRL community. More important from the practical point of view however, is the achievement of an exponential gain sufficiently high to reach the saturation intensity, above which the energy stored in the amplification media

can be efficiently extracted. Currently there are three tabletop soft x-ray laser schemes that have successfully achieved the saturation intensity. Two of these are based on laser pumping schemes. By utilizing pump lasers that produce picosecond and sub picosecond pulses, these schemes have been implemented with apparatus that occupy one to several optical tables rather than an entire research facility as was demanded by the first generation of soft x-ray lasers.

The first of the laser pumping schemes described below uses a very short pulse laser pump to ionize the plasma by optical field induced ionization. In optical field induced ionization (OFI), electrons tunnel through the barrier of the host atom due to the interaction with a very intense externally applied electric field. Very intense electric fields can be obtained by using extremely short laser pulses. The excess energy of the electrons after ionization due to their interaction with the laser pulse has become known as above threshold ionization (ATI). Burnett and Corkum determined that this excess energy is a result of a phase mismatch between the time of ionization and the crest of the electromagnetic wave [1.19,1.20]. Depending on the polarization of the light, two different situations can arise. If linearly polarized light is used, ionization of the species occurs near the peak of the electromagnetic wave and the phase mismatch is minimized resulting in an abundance of cold free electrons present after ionization. On the other hand, the total electric field for circularly polarized light will always have a component that results in a maximum phase mismatch, thus, an abundance of hot electrons can exist after ionization. Because of these two situations, OFI is attractive for both recombination schemes as well as collisional excitation schemes.

In 1994, a group from Stanford University using OFI in an electron-collision

excitation scheme observed lasing at 41.8 nm in Pd-like Xe. The experiment was performed using a circularly polarized Ti:sapphire laser operating at 800 nm in a chirped pulse regime to produce 40 fs, 70 mJ laser pulses with a repetition rate of 10 Hz. The laser beam was focused into a Xe cell pressurized between 5 and 12 torr. The intensity of the laser pulse was sufficient to tunnel ionize the Xe while simultaneously producing the hot electrons necessary to collisionally excite the Pd-like ionic ground state to the laser upper level. Lemoff et al. reported a gain coefficient of  $13 \text{ cm}^{-1}$  and an overall gain of  $\cong \exp(11)$  [1.21]. This was the first successful demonstration of a laser pumped scheme that did not require a solid target and was the first to operate as fast as 10 Hz. However, the output energy obtained was small and insufficient for most applications. Recently, utilizing the same OFI scheme and increasing the laser pump energy from 70 mJ to 330 mJ, a French group succeeded in saturating this Pd-like Xe laser [1.22]. They reported saturated output at a gain length product of 15 and a total photon output under saturated conditions of  $5 \times 10^9$  photons/pulse. This corresponds to an energy of  $\cong 24 \text{ nJ}$  per pulse and an average power of  $0.24 \text{ }\mu\text{W}$  when running at 10 Hz.

Another laser pump scheme that uses OFI was demonstrated in 1993 at the RIKEN institute in Japan. However, this scheme used OFI for the production of an ionized plasma with cold free electrons for excitation by collisional recombination. Nagata et al. [1.23] reported the first observation of amplification on the Lyman- $\alpha$  transition of hydrogenic lithium at 13.5 nm using this scheme. Corkum and Burnett theoretically realized the feasibility of this scheme to produce a population inversion with respect to the ground state of the ion [1.19, 1.20]. A population inversion with respect to the ground state is very attractive because the  $n=2$  to  $n=1$  transition has a photon energy

5.4 times greater than that of the  $n=3$  to  $n=2$  transition. As a consequence of this OFI scheme, a plasma is produced with fully stripped Li III and cold free electrons which is optimum for a rapid three body recombination. The subsequent cascade of the electrons results in a large population inversion with respect to the ground state of the ion.

While the RIKEN group was able to achieve a small signal gain of  $20 \text{ cm}^{-1}$ , they were unable to produce a plasma with the required temperature and density for lengths longer than 2 mm. The resulting overall gain was only  $\exp(4)$  which does not clearly demonstrate the non-linear gain of the amplifier. Similar experiments conducted at Berkeley/Livermore [1.24] and Princeton [1.25] with slightly different setups were able to reproduce the RIKEN results, but again were unable to observe a gain-length (gl) product larger than four. More recently however, Korobkin et al. at Princeton University devised a method that produced an appropriate plasma in a microcapillary waveguide for lengths up to 5 mm. Using a Nd/YAG laser (100 mJ, 5 ns) focused on the entrance of a microcapillary made of LiF, an initial plasma of singly ionized Li was produced in the channel. A subsequent laser pulse (50-60 mJ, 250 fs) tightly focused into the plasma produced the Li III plasma by OFI. They reported a small signal gain of  $11 \text{ cm}^{-1}$  and an overall gain of  $\exp(5.5)$  at 13.5 nm in Li III [1.26]. However, the OFI recombination laser scheme has not yet been able to achieve gain saturation and a larger gl is needed to turn this potentially efficient laser into a practical device.

The other laser pumping scheme that has succeeded in reaching saturation takes advantage of the very large transient inversions that can be obtained using ultrashort pulse laser excitation. An early experiment conducted at the Max Born Institute in Germany using a powerful picosecond laser pump resulted in a gain of  $\exp(9.5)$  in

Ne-like Titanium at 32.6 nm [1.27]. This pumping scheme, described as the transient collisional scheme, is based on a two-step laser pumped excitation method that produces a transient population inversion rather than operating in a quasi steady-state regime. As is typical with most laser pumped schemes, this experiment was done using a solid density target. A 1.5 ns, 7 J, laser pulse at 1053 nm was line focused on to the target to generate a plasma with the correct density, temperature and an abundance of Ne-like Ti ions. A second 4 J laser pulse with a duration of less than 0.7 ps was then used to heat the plasma to a temperature  $T_e > \Delta u$  ( $\Delta u$  is the energy difference to the laser upper level) for efficient excitation of the Ne-like ions to the laser upper level via electron collisions. By selectively populating the laser upper level in a short time as compared to the radiative and collisional relaxation times, a non-stationary population inversion was created. Because of the rapid excitation, a very high gain coefficient can be achieved. Nickles *et al.* reported a gain coefficient of  $19 \text{ cm}^{-1}$  for an overall plasma length of 5 mm [1.27]. Unfortunately, the transient gain lifetime is on the same order as the propagation time through a 2 mm long plasma making it difficult to produce longer amplifying plasmas. Recently, work conducted at Lawrence Livermore National Laboratory overcame the inherent barrier of the transient gain, extended this transient collisional scheme to several other Ni-like ions and achieved gain saturation. Dunn *et al.* have observed gain saturation with plasma column lengths up to 1 cm by utilizing a traveling wave excitation method. Using a simple reflection echelon, the wave front of the pump laser was segmented and consecutively delayed such that the phase velocity in the plasma was matched by the delay between segments. They reported a gain coefficient of  $62 \text{ cm}^{-1}$  and a gain length product of 18 with an output pulse energy of  $12 \mu\text{J}$  for the Ni-like Pd

line at 14.7 nm [1.28]. Using this scheme, they were also able to slightly reduce the required laser pump energies of the two pulses to a total of 5–7 J. The transient collisional excitation scheme is very attractive for tabletop x-ray lasers due to the relatively low pump energies and the potential for this scheme to allow lasing near the "water-window" region in Ni-like ions with only tens of joules pump energy [1.29].

#### **1.4. Capillary discharge approach to SXRLs**

As a solution for the development of practical soft x-ray lasers, our group at Colorado State University has been developing a tabletop soft x-ray laser scheme, first proposed in 1988 [1.30], that is based on a direct electrical discharge through a capillary filled with a pre-ionized plasma. The first demonstration of large soft x-ray amplification based on a fast capillary discharge pumped scheme was in 1994 on the J=0-1 transition in Ne-like Ar at 46.9 nm [1.31]. Later, the saturation limit for this transition was achieved [1.32] and lasing in Ne-like S [1.33] and Ne-Like Cl [1.34] has also been observed using this scheme.

In our scheme, the plasma column is created by a fast current pulse that flows between two electrodes at each end of a capillary channel. The capillary geometry has the benefit of high initial plasma symmetry, high axial uniformity and small initial diameter. The current pulse produces a magnetic field, which rapidly compresses the plasma column to form a very hot and dense plasma. Just before maximum compression, the plasma reaches the necessary density and temperature to produce lasing by collisional excitation of multiply ionized argon atoms. At this time the plasma column has a very large aspect ratio, that in the experiments described in this work reached 1000:1. These conditions are very desirable for large amplification. The small diameter and significant

radial plasma velocity variation is beneficial in building a large population inversion by allowing the radiation from the laser lower level to escape radially, while the long length obviously gives a large amplification.

Initial parameterization of the 46.9 nm transition showed that a laser pulse could be generated for an argon pressure between 500 and 750 mTorr in a 4 mm diameter, polyacetal capillary for a discharge current pulse with a peak current between 34 and 41 kA and a 60 ns first half cycle [1.35]. The discharge for this initial experiment was designed to be versatile to obtain the operating parameters for the 46.9 nm transition as well as to investigate other discharge created plasmas. Therefore, the discharge and charging system could generate peak currents that far exceeded the requirements of the 46.9 nm transition. The next logical step in the progression of these lasers and was the focus of this author's Masters Thesis was to design a discharge that was specifically for this transition in an effort to reduce the size, increase the repetition rate and create a device that could be used for applications.

## **1.5. Previous work**

In this author's previous work, a soft x-ray laser was developed that was based on the capillary discharge scheme and had been optimized for the 46.9nm transition in Ne-like Ar. This resulted in the first table-top soft x-ray laser of size comparable to that of many widely utilized commercially available visible and ultra-violet sources that was capable of producing micro-joule level laser pulse energies [1.2]. This device used polyacetal capillaries and was electrically similar to its predecessor. The design differed mainly in the final stage of the current pulse generation. In this design a coaxial Blumlein transmission line was directly discharged across the capillary and a four stage

Marx generator was used to pulse charge the Blumlein transmission line. The voltage amplification effect of the Blumlein design allows the main discharge body to be physically compact. The discharge is shown in figure 1.1 next to a 5 mW He-Ne laser. The optimization of the laser showed that pulse energies of 25  $\mu\text{J}$  were possible with 18.6cm long capillaries at an optimum argon pressure of 600 mTorr, a capillary diameter of 4 mm and a peak discharge current of 37 kA. Figure 1.2 shows the measured laser pulse energy under optimized conditions for capillary lengths between 8.7 cm and 18.6 cm. Previous measurements of a similar capillary discharge laser resulted in a small signal gain coefficient of  $1.16 \text{ cm}^{-1}$  [1.32] and can be expected to be approximately the same in this amplifier. This corresponds to a  $g > 16$  for the longest capillaries where the intensity is sufficient to saturate the plasma column.

Repetition rate and continuous operation lifetime measurements were also made. Electrically, the system was designed to operate at repetition rates upwards of 10Hz. However, due to the limitations of the polyacetal capillaries, which are strongly ablated by the plasma, lasing was observed at maximum repetition rates of around 1 shot every 30 seconds. Figure 1.3 shows the shot-to-shot laser output intensity fluctuations from a 12.4 cm long capillary fired continuously at 30 second intervals. The fluctuations in the intensity are more a result of variations in the formation of the plasma column than a consequence of shot to shot variations in the peak magnitude of the current pulse. The laser output power was observed to slowly decrease as a function of the number of shots in a new capillary, as the capillary deteriorates with use due to discharge ablation of the walls. High output power was typically obtained for the first 50 to 100 shots in a new capillary. Nevertheless, lasing at degraded output energies was observed for up to at least

300 shots.

The limitation on the repetition rate is due to the accumulation of material in the capillary channel ablated from the walls of the capillary during the discharge. For these measurements, argon gas was injected and evacuated at the same end of the capillary channel. Using this closed capillary channel configuration assures that the argon density will be uniform throughout the length of the capillary. However, it also means that longer pumping times are required between discharges. Preliminary experiments were performed where argon gas flowed through the capillary channel by injecting gas at both ends with a slight pressure drop across the capillary. This experiment showed that while pumping times were reduced and repetition rates could be increased slightly, there was a degradation of the laser pulse energy as a result of the non-uniform initial argon pressure in the capillary.

Given the limitation of the pumping scheme, the only way to drastically increase the repetition rate of the laser is to reduce the amount of ablated material that is introduced from the walls of the capillary during a discharge. Alumina ( $\text{Al}_2\text{O}_3$ ) tubes with inner diameters of around 1 mm to 4 mm are commercially available with various wall thicknesses. Initial experiments were performed using these tubes pressed length wise into Teflon capillary bodies to form ceramic insert capillaries. Results showed that lasing was possible at repetition rates on the order of 1 Hz, however, the  $\sim 100$  J of energy from each electrical discharge being dissipated in the capillary channel quickly melted the Teflon jacket and prohibited further lasing.

Finally using this same discharge, preliminary experiments were performed where the thin wall ceramic capillary was used directly in contact with the liquid dielectric that

filled the discharge. Lasing was observed at the higher repetition rates however, as expected, without protection of the Teflon jacket the capillaries were quickly destroyed by the high electric fields across the capillary walls causing pin-hole fractures. These experiments also showed that the optimum conditions for lasing with ceramic capillaries were significantly different than those for poly-acetal capillaries and led to the design of a new discharge. This next generation capillary discharge laser is discussed in chapter two.

### **1.6. Alternatives to SXRLs for the generation of coherent soft x-ray radiation**

For completeness, it should be mentioned that direct amplification of radiation with x-ray lasers is not the only approach for generating coherent soft x-ray radiation. Currently the most widely utilized source for coherent soft x-rays is that of undulator radiation at synchrotron facilities. At these facilities there are typically many undulators around an electron storage ring. The electrons undergo transverse motion as dictated by the undulator and emit Bremsstrahlung radiation. Electron bunches are kept at relativistic speeds throughout the ring which allows for quasi-CW operation. The wavelength of this radiation depends strongly on the undulator period and the velocity of the relativistic electron beam, and thus the emitted radiation has the advantage of being highly tunable. With the advent of GeV electron storage rings, it is possible to produce x-rays that are tunable over the majority of the soft x-ray region [1.36]. For example, the Advanced Light Source (ALS) at Lawrence Berkeley Laboratory is able to provide tunable soft x-rays by utilizing a 1.3 GeV storage ring. A temporal structure of 20 ps bursts at 500 MHz and a coherent power of 10 mW around 20 to 50 Å has been reported [1.36]. This is a very good average power; however, for applications requiring high instantaneous brilliance, this translates into only a few  $10^5$  photons per pulse. Also, the very large size

and cost of synchrotron facilities encourages the development of more compact coherent soft x-ray sources.

Another alternative to direct lasing action and more compact approach than the synchrotron has been demonstrated using frequency up conversion. High-order harmonic generation has been demonstrated in rare gases using a variety of femto-second and pico-second lasers. In 1982, C. K. Rhodes at the University of Chicago demonstrated for the first time, coherent soft x-ray radiation at 64 nm by frequency tripling a 193 nm, 10 ps source with a conversion efficiency of  $2 \times 10^{-5}$  [1.37]. More recently, the generation of very high order harmonics has been observed. Macklin, Kmetec, and Gordon detected up to the 109<sup>th</sup> harmonic in Ne using a 125 fs Ti:sapphire laser at 806 nm [1.38]. L'Huilier and Balcou used a 1 ps Nd-glass laser to generate the 29<sup>th</sup>, 57<sup>th</sup> and up to at least the 135<sup>th</sup> (160 eV) harmonics in Xe, Ar and Ne respectively [1.39]. To date, the highest order discrete harmonic peak observed was the 221<sup>st</sup> harmonic of a 26 fs pulse, 800 nm Ti:sapphire laser [1.40]. Chang *et al.* observed the 2.7 nm (460 eV) harmonic in He. In contrast, the highest pulse energy generated in a high order harmonic pulse to date is 60 nJ at a photon energy of about 50 eV, and corresponds to an experiment done using the second harmonic of a powerful Nd-glass laser system [1.41]. These results clearly demonstrate the feasibility of using high-order harmonic generation for the production of coherent x-rays in sufficient quantity to be used in several applications. However, the generally low yield of photons, due to the poor conversion efficiencies [1.38, 1.39, 1.42], has been an obstacle for practical applications. At present, the generation of high order harmonics under fairly optimized non-phased matched conditions typically yields a conversion efficiency of about  $10^{-6}$  in the photon energy range of 10-40 eV (of the order

of  $10^9$  photons per pulse) [1.43]. Recently a very important advance in this field was accomplished with the demonstration of phase-matched harmonic conversion of visible light into soft x-rays [1.44]. A conversion efficiency of  $10^{-5}$ - $10^{-6}$  was obtained in the 40-70 eV spectral region. Soft x-ray pulses with an energy of  $> 0.2$  nJ per harmonic order were produced at a repetition frequency of 1kHz, corresponding to an average power of  $> 0.2$   $\mu$ W [1.44]. This result is significant because further optimization of this technique could result in the generation of high average power beams of spatially coherent soft x-ray radiation from a table-top optical laser.

## 1.7. Figures

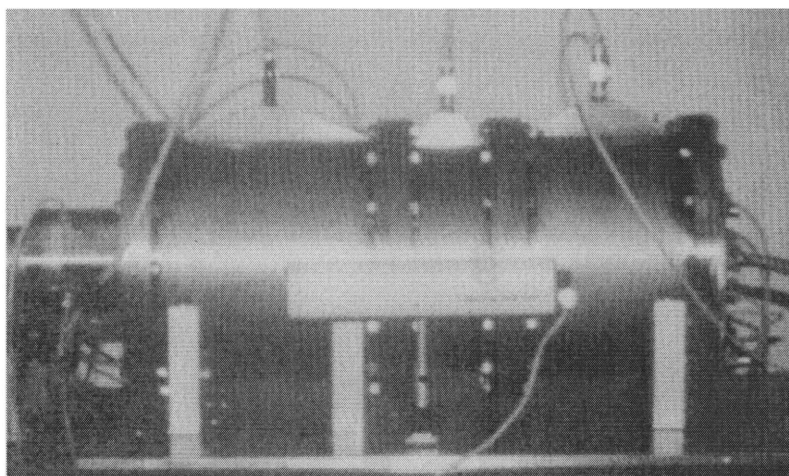


Figure 1.1. Size of the 46.9 nm laser (back) relative to a 5 mW He-Ne laser (front).

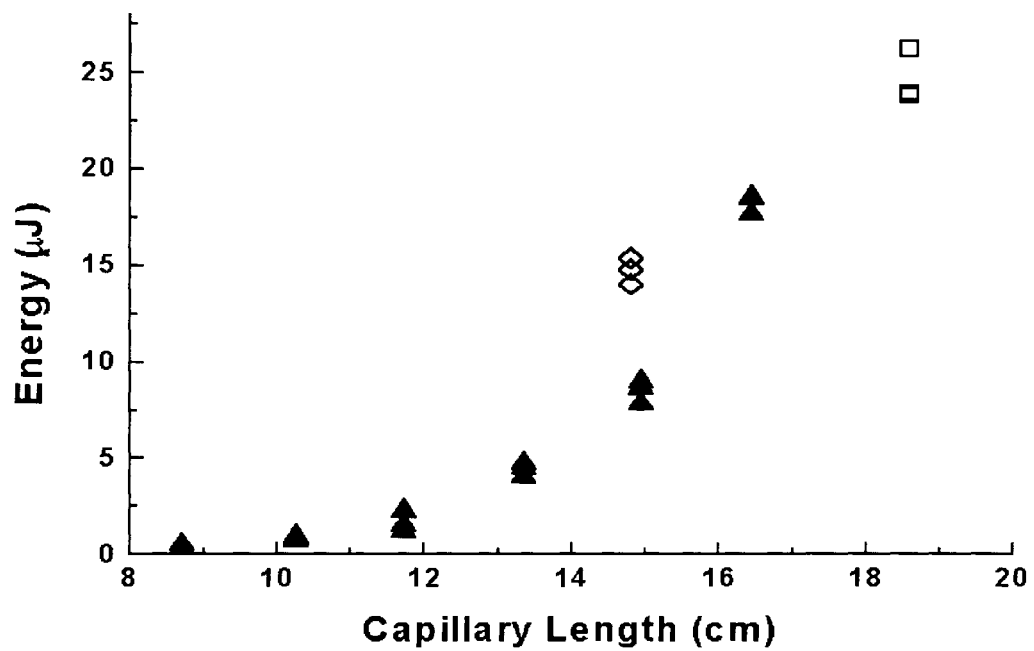


Figure 1.2. Laser output energy produced with capillaries of various lengths. The best three shots obtained for each capillary length are shown. Average values are lower. Different symbols represent shots in different capillaries.

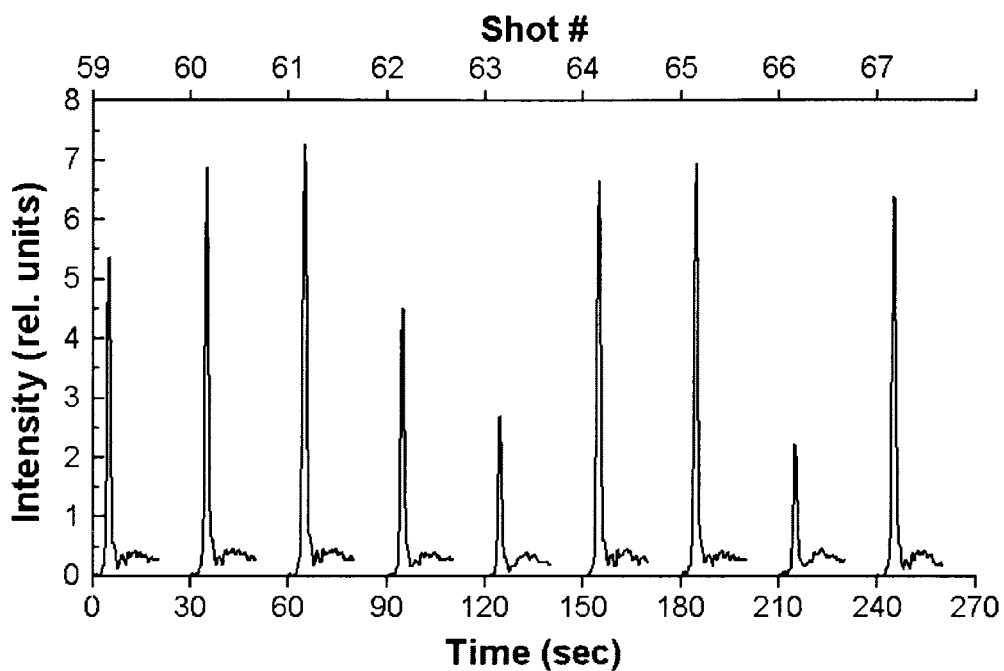


Figure 1.3. Laser output obtained from a 12.4 cm long capillary, firing the discharge at 30 second intervals. The shot number identifies the number of shots in the same capillary.

## 1.8. References

- [1.1] J.J. Rocca, V. Shlyaptsev, F.G. Tomasel, O.D. Cortazar, D. Hartshorn, and J.L.A. Chilla, *Phys. Rev. Lett.* **16**, 2192 (1994).
- [1.2] B.R. Benware, C.H. Moreno, D.J. Burd and J.J. Rocca, *Opt. Lett.*, **22**, 796 (1997).
- [1.3] F.G. Tomasel, J.J. Rocca, V.N. Slyaptsev, and C.D. Macchietto, *Phys. Rev. A* **55**, 1437 (1997)
- [1.4] D. Attwood, K. Halbach, K. J. Kim, *Science* **228**, 1265 (1985).
- [1.5] D. Attwood, *Phys. Today* **45**, 24 (1992).
- [1.6] S. Svanberg, and C. G. Wahlstrom, eds., *Proceedings of the Fifth International Conference on X-Ray Lasers* (Institute of Physics, Bristol, UK, 1996).
- [1.7] C. H. Skinner, D. S. Diccico, D. Kim, R. J. Rosser, S. Suckewer, A. P. Gupta, and J. G. Hirshberg, *J. Microsc.* **159**,51 (1990).
- [1.8] L. B. DaSilva et al., *Science* **258**, 269 (1992).
- [1.9] J. E. Trebes et al., *Science* **238**, 517 (1987).
- [1.10] L. B. Da Silva et al., *Phys. Rev. Lett.* **74**, 3991 (1995); A.S.Wan, T.W. Barbee Jr., R. Cauble, P. Celliers, L. B. Da Silva, J. C. Moreno, P. W. Rambo, G. F. Stone, J. E. Trebes, and F. Weber, *Phys. Rev. E* **55**, 6293 (1997).
- [1.11] R. Cauble, L. B. Da Silva, T. W. Barbee Jr., P. Celliers, J. C. Moreno, and A. S. Wan, *Phys. Rev. Lett.* **74**, 3816 (1995).
- [1.12] P. Jaegle' et al., *J. Appl. Phys.* **81**, 2406 (1997); G. Jamelot et al., in *Soft X-ray Lasers and Applications II*, edited by J. J. Rocca and L. B. Da Silva, *Proc. SPIE* (Society of Photooptical Engineers, Bellingham, WA, 1997), Vol. 3156., p. 124.
- [1.13] T. Tomie, H. Kondo, and H. Shimizu in *X-ray Lasers 1996*, eds. S. Svanberg and C.G. Wahlstrom (IOP Conf. Proc., Lund, Sweden, 1996), p. 520.
- [1.14] L.B. Da Silva, T.W. Barbee, Jr., R.Cauble, P. Celliers, C.D. Decker, D.H. Kalantar, M.H. Key, R.A. London, J.C. Moreno, J.E. Trebes, A.S. Wan and F. Weber, in *X-ray Lasers 1996*, eds. S. Svanberg and C.G. Wahlstrom (IOP Conf. Proc.,Lund, Sweden, 1996), p. 496.

- [1.15] J. Filevich, K. Kanizay, M.C. Marconi, J.L.A. Chilla and J.J. Rocca, *Opt. Lett.* **25**, 356 (2000).
- [1.16] M.C. Marconi, C.H. Moreno, J.J. Rocca, V.N. Shlyaptsev, and A.L. Osterheld, *Phys. Rev. E* **62**, 7209 (2000)
- [1.17] D. L. Matthews, P. L. Hagelstein, M. D. Rosen, M. J. Eckart, N. M. Ceglio, A. N. Hazi, M. Medecker, B. J. MacGowan, J. E. Trebes, B. L. Whitten, E. M. Cambell, C. W. Hatcher, A. M. Hawryluk, R. L. Kaufman, L. P. Pleasance, G. Rambach, J. H. Scofield, G. Stone, and T. A. Weaver, *Phys. Rev. Lett.* **54**, 110 (1985).
- [1.18] S. Suckewer, C. H. Skinner, H. Milchberg, C. Keane, and D. Voorhees, *Phys. Rev. Lett.* **55**, 1753 (1985).
- [1.19] N.H. Burnett and P.B. Corkum, *J. Opt. Soc. Am. B* **6**, 1195 (1989).
- [1.20] P.B. Corkum and N.H. Burnett in *“Short Wavelength Coherent Radiation: Generation and Applications”*, edited by R.W. Falcone and J. Kirz (OSA, North Falmouth, MA, 1988), vol. 2, p. 225.
- [1.21] B.E. Lemoff, G.Y. Yin, C.L. Gordon III, C.P.J. Barty, and S.E. Harris, *Phys. Rev. Lett.* **74**, 1574 (1995).
- [1.22] S. Sebban, R. Haroutunian, Ph. Balcou, G. Grillo, A. Rousse, S. Kazamias, T. Marin, J.P. Rousseau, L. Notebaert, M. Pittman, J.P. Chambaret, A. Antonetti, D. Hulin, D. Ros, A. Klisnick, A.Carillon, P. Jaegle, G. Jamelot, and J.F. Wyart, *Phys. Rev. Lett.* **86**, 3004 (2001).
- [1.23] Y. Nagata, K. Midorikawa, M. Obara, H. Tashiro, and K. Toyoda, *Phys. Rev. Lett.* **71**, 3774 (1993).
- [1.24] T. Donnelly et al., in *Proceedings of the Fourth International Conference on X-Ray Lasers*. Williamsburg, VA, 1994, edited by D. Eder and D. Matthews AIP Conf. Proc. No. 332 (AIP, New York, 1994), p. 106.
- [1.25] K. Krushelnick, W. Tighe, and S. Suckewer, *J. Opt. Soc. Am. B* **13**, 306 (1996).
- [1.26] D.V. Korobkin, C.H. Nam, and S. Suckewer, *Phys. Rev. Lett.* **26**, 5206 (1996).
- [1.27] P.V. Nickles, V.N. Shlyaptsev, M. Kalacknikov, M. Schnurer, I. Will, and W. Sandner, *Phys. Rev. Lett.* **78**, 2748 (1997).
- [1.28] J. Dunn, Y. Li, A.L. Osterheld, J. Nilsen, J.R. Hunter, and V.N. Shlyaptsev, *Phys.*

- Rev. Lett. **84**, 4834 (2000).
- [1.29] V.N. Slyaptsev, P.V. Nickles, T. Schlegel, M.P. Kalashnikov, and A.L. Osterheld, SPIE **2012**, 111 (1993).
- [1.30] J.J. Rocca, D.C. Beethe, and M.C. Marconi, Opt. Lett. **13**, 565 (1988).
- [1.31] J.J. Rocca, V. Shlyaptsev, F.G. Tomasel, O.D. Cortazar, D. Hartshorn, and J.L.A. Chilla, Phys. Rev. Lett. **16**, 2192 (1994).
- [1.32] J.J. Rocca, D.P. Clark, J.L.A. Chilla, and V.N. Shlyaptsev, Phys. Rev.Lett. **8**, 1467 (1996).
- [1.33] F.G. Tomasel, J.J. Rocca, V.N. Shlyaptsev, and C.D. Macchietto, Phys. Rev. A **55**, 1437 (1997).
- [1.34] M. Frati, M. Seminario, and J.J. Rocca, Opt. Lett. **25**, 1022 (2000).
- [1.35] J.J. Rocca, F.G. Tomasel, M.C. Marconi, V.N. Slyaptsev, J.L.A. Chilla, B.T. Szapiro, and G. Guidice, Phys. Plasmas **2**, 2547 (1995).
- [1.36] D. Attwood, G. Sommargren, R. Beguiristain, K. Nguyen, J. Bokor, N. Ceglio, K. Jackson, M. Koike, J. Underwood, Appl. Opt. **32**, 7022 (1993).
- [1.37] C.K. Rhodes, AIP Conf. Proc. **90**, 112 (1982).
- [1.38] J. J. Macklin, J. D. Kmetec, and C. L. Gordon III, Phys. Rev. Lett. **70**, 766 (1993).
- [1.39] A. L'Huilier, and Ph. Balcou, Phys. Rev. Lett. **70**, 774 (1993).
- [1.40] Z. Chang, A. Rundquist, H. Wang, M.M. Murnane, and H. Kapteyn, Phys. Rev. Lett. **79**, 2967 (1997).
- [1.41] T. Ditmier, J.K. Crane, H. Nyugen, L.B. Da Silva and M.D. Perry, Phys.Rev.A., **51**, R902 (1995).
- [1.42] J. F. Reintjes, "Coherent Ultraviolet and Vacuum Ultraviolet Sources," in Laser Handbook, M. Bass and M. L. Stitch, eds. (North-Holland, New York, 1985).
- [1.43] A. LHuillier in X-Ray Lasers 1996, edited by S. Svanberg and C.G. Wahlstrom (Inst. of Phys., Bristol, 1996), p. 444.
- [1.44] A. Rundquist, C.G. Durfee III, Z. Chang, C. Herne, S. Backus, M.M. Murnane and H.C. Kapteyn, Science, **280**, 1412 (1998).

## CHAPTER 2

### HIGH AVERAGE POWER, HIGH REPETITION RATE TABLE TOP SOFT X-RAY LASER OPERATING AT 46.9nm

#### 2.1. Introduction

X-ray lasers pumped by large optical lasers of the type used in fusion research have generated output pulse energies of up to several mJ [2.1]. However as discussed in the previous chapter, these lasers are limited to a repetition frequency of only a few pulses per hour at best. Recently, significant progress has been accomplished in the development of more compact soft x-ray lasers that can operate at increased repetition frequencies [2.2, 2.3, 2.4, 2.5, 2.6, 2.7]. However, in all the lasers previous to this work, the average power has been low, as a result of either a low repetition rate or a low energy per pulse. An important step in the development of practical table-top soft x-ray lasers is the generation of high average output powers, which simultaneously requires a high repetition rate and a high energy per pulse. This chapter details the first demonstration and characterization of a high average power table-top soft x-ray laser. An average power of ~3.5 mW was generated at 46.9 nm. This value exceeds the average powers obtained to date with table-top soft x-ray lasers by 2 to 3 orders of magnitude. The capillary discharge-pumped laser reported herein occupies an area of approximately 0.4 m × 1 m on top of a table, a size comparable to that of many widely utilized visible or

ultraviolet gas lasers.

## **2.2. Development of the high average power table-top SXRL**

In capillary discharges the amount of material ablated from the walls by plasma radiation and electron heat conduction can greatly affect the plasma compression and heating. In the polyacetal capillaries utilized in previous discharge-pumped collisional soft x-ray laser experiments, 20 to 50% of the  $\approx 39$  kA discharge current necessary to excite Ne-like Ar is computed to flow through material ablated from the walls [2.8]. This significantly reduces the efficiency of the plasma compression. In the experiment described herein,  $\text{Al}_2\text{O}_3$  capillaries were used that are much more resistant to ablation and also have a larger heat conductivity that allows for the dissipation of high average discharge powers. An indication of the dramatic reduction in the mass of ablated material in the ceramic capillaries as compared to the poly-acetal capillaries is the much smaller pressure increase measured at the exit of the capillary channel following a discharge shot:  $<10$  mTorr instead of several Torr. This reduced wall ablation in ceramic capillaries results in a more efficient use of the current pulse, which allows for a significantly lower excitation current and for operation at high repetition rates.

The discharge setup and pulse generator used in this experiment resemble those described in the literature [2.7, 2.9, 2.10]. The fast current pulse that creates the necessary plasma conditions is generated by discharging a water capacitor through a spark gap switch connected in series with the capillary load. The water served as a liquid dielectric for the capacitor and also cooled the capillary. The capacitor was pulse-charged by a four-stage Marx generator that is enclosed in a separate box and connected to the laser head with a coaxial cable. The coaxial capacitor design of the main discharge

allowed for a capacitance range of  $<5$  nF to up to 20 nF. A 50 kV, 10 kJ constant current capacitor charging power supply was used and is capable of charging the Marx generator in less than 50 ms and thus, the electrical system is limited to just over 20 Hz repetition rate. A pre-ionization circuit was provided to uniformly pre-ionize the argon gas prior to excitation with the fast high current pulse. Given the temporal constraints of the fast current pulse and the inductive load of the capillary, a capillary length of about 36 cm under optimized lasing conditions reaches the electrical limits of the system regardless of the repetition rate due to the maximum voltage constraints of the power supply and the main discharge capacitor. For this reason, the laser was operated with capillary lengths ranging from 18 cm to 36 cm. Figure 2.1 shows a picture of the main discharge head that houses the capillary with the attached vacuum pumping system.

### **2.3. Measurement of laser pulse energy**

Lasing with an average power of 0.95 mW at a wavelength of 46.9 nm was obtained by exciting pre-ionized Ar filled alumina capillaries 3.2 mm in diameter and 18.2 cm in length, with a current pulse having an amplitude of  $\approx 24$  kA, a 10 to 90% risetime of  $\approx 25$  ns and a first half-cycle duration of  $\approx 110$  ns. A nearly optimum Ar gas pressure of 490 mTorr was maintained in the capillary using a continuous Ar flow and a differential pumping system.

To determine the average output power the laser output pulse energy was measured for every shot using a vacuum photodiode placed at 87 cm from the exit of the laser. The data were recorded and stored by a 2 GSa/s digitizing oscilloscope with 500 MHz analog bandwidth. The quantum efficiency of the Al photocathode was previously

calibrated with respect to a silicon photodiode of known quantum yield [2.8]. The laser output was attenuated with several stainless steel meshes of measured transmissivity to avoid saturation of the photodiode. The laser was successfully operated at repetition frequencies up to 10 Hz. However, the most detailed optimization was performed at 7 Hz, resulting in the highest average power at this lower frequency. Figure 2.2 shows the measured laser output pulse energy and average power at 7 Hz repetition frequency at the near-optimum discharge pressure of 490 mTorr. The data corresponds to 1 minute of continuous operation of the laser. Figure 2.2a and 2.2c show that the average output energy per pulse is  $135 \mu\text{J} \pm 17 \mu\text{J}$ , and figure 2.2b shows that the average power at 7 Hz is 0.95 mW. This corresponds to  $> 2.2 \times 10^{14}$  photons per second. The laser was operated uninterruptedly during 30 minutes at 5 Hz and  $9 \times 10^3$  laser shots from a single capillary have been accumulated. After this number of shots lasing was still observed, but the output pulse energy degraded to about half its maximum value due to deterioration of the capillary walls.

To determine the peak intensity, the laser pulse-width was measured using a vacuum photodiode and an analog oscilloscope with 1 GHz bandwidth. The measurements were corrected by taking into account the limited frequency response of the oscilloscope. Figure 2.3 shows the temporal profile of a typical laser pulse. The full width at half maximum pulsewidth of the laser pulses generated at 7 Hz was measured to be  $\approx 1.2$  ns. The laser pulsewidth was measured to be slightly larger at 1 Hz,  $\approx 1.3$  ns. The small reduction of the laser pulsewidth with increased repetition rate is most likely associated with a reduction of the density of Ar atoms in the capillary channel as a result of increased gas heating. This is supported by measurements that showed a decreased

laser pulsewidth at reduced Ar pressures. The peak power of a typical laser pulse is  $\approx 112$  kW, while the peak power of the most intense shots exceed 150 kW.

#### **2.4. Operation of the laser in a highly saturated regime**

The 18 cm long capillaries used to obtain the results above are only slightly longer than the 14 - 15 cm at which gain saturation was observed and moderate reductions in the capillary length would dramatically reduce the laser pulse energies obtained. On the other hand, increased laser output energy may be achieved by double-pass amplification using a mirror placed in close proximity to the end of the plasma column [2.1, 2.9]. However, rapid damage of the mirror by the plasma makes this solution unsuitable for high repetition rate operation [2.9]. Instead, the results reported herein were obtained by increasing the length of the plasma column to 34.5 cm, a length more than twice the saturation length. The length to diameter ratio of this plasma column exceeds 1000:1, and is to the knowledge of the Author the largest used to date in soft x-ray laser research. Operation in this highly gain-saturated amplification regime allows for the efficient extraction of the energy stored in the population inversion from the majority of the amplifier volume. Laser pulses with an average energy of 0.88 mJ ( $> 2 \times 10^{14}$  photons/pulse) were generated at a wavelength of 46.9 nm at a repetition frequency of 4 Hz, while the energy of the most intense pulses exceeded 1 mJ. The average power obtained was 3.5 mW, the highest reported to date for a table-top soft x-ray laser.

Figure 2.4 shows the average laser output pulse energy obtained utilizing capillary plasma columns of 16, 25 and 34.5 cm in length. The laser average output pulse energy was measured to increase from 0.075 mJ for a plasma column 16 cm in length, to 0.88 mJ

for the plasma column 34.5 cm in length. Estimates of the laser intensity based on these energies and on the pulsewidth measurements discussed below indicate that the saturation intensity of 56-78 MW/cm<sup>2</sup> [2.9] is exceeded before the end of the 16 cm capillary, and that the output of the longest capillary exceeds the saturation intensity by more than an order of magnitude, approaching 1 GW/cm<sup>2</sup>. Figure 2.5a shows the shot to shot variations of the measured laser output pulse energy and corresponding laser average power for the 34.5 cm long discharge operated at 4 Hz repetition frequency. The data corresponds to 100 seconds of uninterrupted operation of the laser. The solid line shows that the average laser power is about 3.5 mW, corresponding to  $> 8 \times 10^{14}$  photons per second. Figure 2.5b shows that the average laser output energy per pulse is 0.88 mJ and that the energy of the highest energy pulses exceeds 1 mJ. More than 5000 laser shots were obtained from a single capillary.

The temporal evolution of the laser pulse for this 34.5 cm long capillary was measured with a fast vacuum photodiode and a 1 GHz bandwidth analog oscilloscope. A typical laser output pulse corresponding to the 34.5 cm long amplifier is shown in figure 2.6. The full width at half maximum of the laser pulse is determined to be 1.5 +/- 0.05 ns by correcting the measured pulse for the limited bandwidth of the detection system. This laser pulse-width is longer than the 1.2 ns that was measured for an 18.2 cm long amplifier. The increase of the laser pulse-width is the result of the increased transit time of the radiation through the amplifier. Taking into consideration this pulse-width, the average peak laser output power obtained with the longest plasma column is estimated to be  $\approx 0.6$  MW.

## 2.5. Measurement of the far field beam profile

The far field laser output intensity distributions corresponding to the three capillary plasma lengths of figure 2.4 were measured using a phosphor screen and a CCD array detector of 1024 x 1024 pixels. In all cases the beam profile has a ring shape that is the result of refraction of the rays by plasma density gradients in the plasma column [2.11,2.12]. Figure 2.7 shows cross sections of the output intensity patterns. The measurements are an average of five consecutive laser shots. The peak to peak divergence is about 4.6 mrad in all three cases. The beam profiles are similar for all amplifier lengths, with slightly more pronounced peaks for the longer plasma column lengths. The similarity of the profiles is a consequence of the waveguide nature of the amplifier column. The combination of gain guiding and refraction anti-guiding determines the intensity distribution [2.12], that for the plasma column length of 16 cm is already converging to that of the eigen-mode of the waveguide. From the measured laser beam parameters reported above for the 34.5 cm long amplifier, and assuming a beam diameter of 300  $\mu\text{m}$  at the exit of the laser [2.11], the peak spectral brightness of this laser can be estimated to be  $\approx 1 \times 10^{23}$  photons/(s $\cdot\text{mm}^2 \cdot \text{mrad}^2 \cdot 0.01\%$  bandwidth). This value makes this table-top laser one of the brightest soft x-ray sources to date [2.13].

## 2.6. Comparison of coherent laser output power to a synchrotron beamline

It is of interest to compare the spatially coherent power emitted by this table-top laser to that generated at 26.5 eV in a similar bandwidth by a third-generation synchrotron beam-line. For the purpose of making a comparison of output power per unit bandwidth, the laser linewidth can be conservatively estimated to be  $\Delta\lambda/\lambda = 1 \times 10^{-4}$ . This

results from considering that the Doppler broadened linewidth of the laser transition for an ion temperature of  $T_i \approx 100$  eV [2.8] is about  $\Delta\lambda/\lambda = 1.2 \times 10^{-4}$ , and that it narrows by a factor  $(g^*I_{\text{sat}})^{1/2} \approx 3.7$  as the radiation is amplified to reach saturation at  $g^*I_{\text{sat}} \approx 14$  [2.8]. While some degree of line re-broadening might occur after saturation [2.14], the laser linewidth can be expected to still remain below  $\Delta\lambda/\lambda = 1 \times 10^{-4}$ . Assuming that the spatial coherence of the laser beam produced in the ceramic capillary is similar to that recently measured for a discharge in a polyacetal capillary (about six times diffraction limited in the tangential direction and eight to nine times diffraction limited in the radial direction [2.15]), the average spatially coherent power can be estimated to be about 2% of the 3.5 mW measured, or  $\approx 70$   $\mu\text{W}$ . This spatially coherent power is similar to the  $\approx 20$   $\mu\text{W}$  emitted at this wavelength with  $\Delta\lambda/\lambda = 1 \times 10^{-4}$  by the 8 cm period undulator at the Advanced Light Source, a third generation synchrotron situated at Berkeley [2.16]. Nevertheless, for some applications the synchrotron has the important advantage of broad tunability at shorter wavelengths. In contrast, the peak power of the spatially coherent radiation emitted by the capillary discharge laser is estimated to be about 11.7 kW, and exceeds by more than 6 orders of magnitude that of the undulator, estimated at  $\approx 4$  mW.

## 2.7. Conclusion

In conclusion, the operation of a very compact table-top 46.9 nm laser at an average power of 3.5 mW has been demonstrated. This result corresponds to an increase in the average power available from soft x-ray lasers by 2 to 3 orders of magnitude. The demonstration of a table-top soft x-ray laser with a spatially coherent average power per unit bandwidth similar to that of a synchrotron beam-line has the potential to greatly

expand the use of intense coherent short-wavelength radiation in applications. Table 2.1 summarizes the output characteristics of this laser compared to that of its poly-acetal capillary predecessor.

**Table 2.1**

Laser Parameter	Poly-Acetal [2.7]	Ceramic [this work]	Ceramic [this work]
Capillary Length	18.6 cm	18.2 cm	34.5 cm
Average Pulse energy	25 $\mu$ J single shot	135 $\mu$ J @ 7 Hz	0.88mJ @ 4 Hz
Average Pulse Power	<0.2 $\mu$ W @ 1shot / 2 min.	0.95 mW	3.5 mW
Peak Pulse Power	~40 kW	~113 kW	~0.6 MW
Divergence	2- 5 mrad	4.6 mrad	4.6 mrad
Pulse Width	0.6 – 0.7 ns	1.2 ns	1.5 ns

## 2.8. Figures

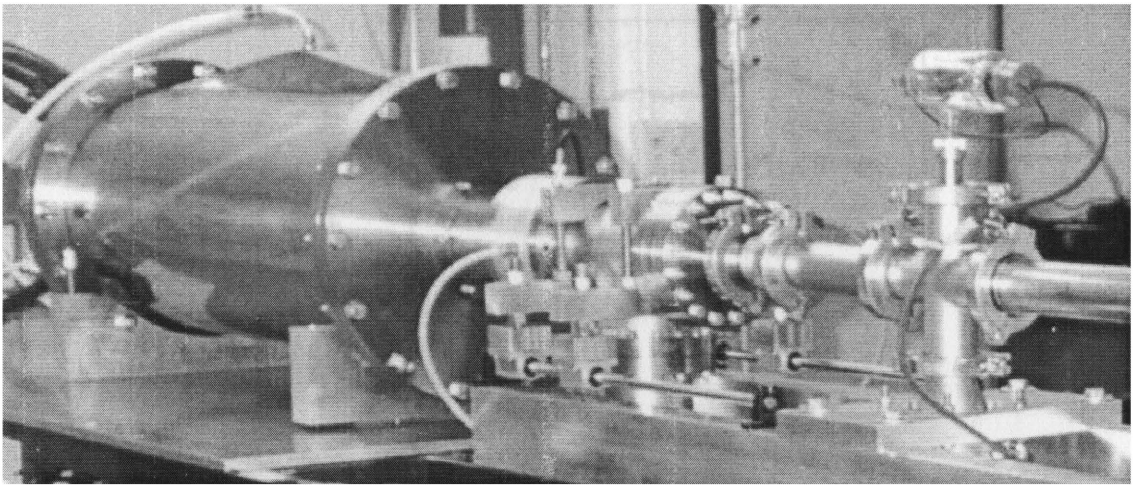


Figure 2.1. Picture of the high average power soft x-ray laser with attached vacuum system in the foreground.

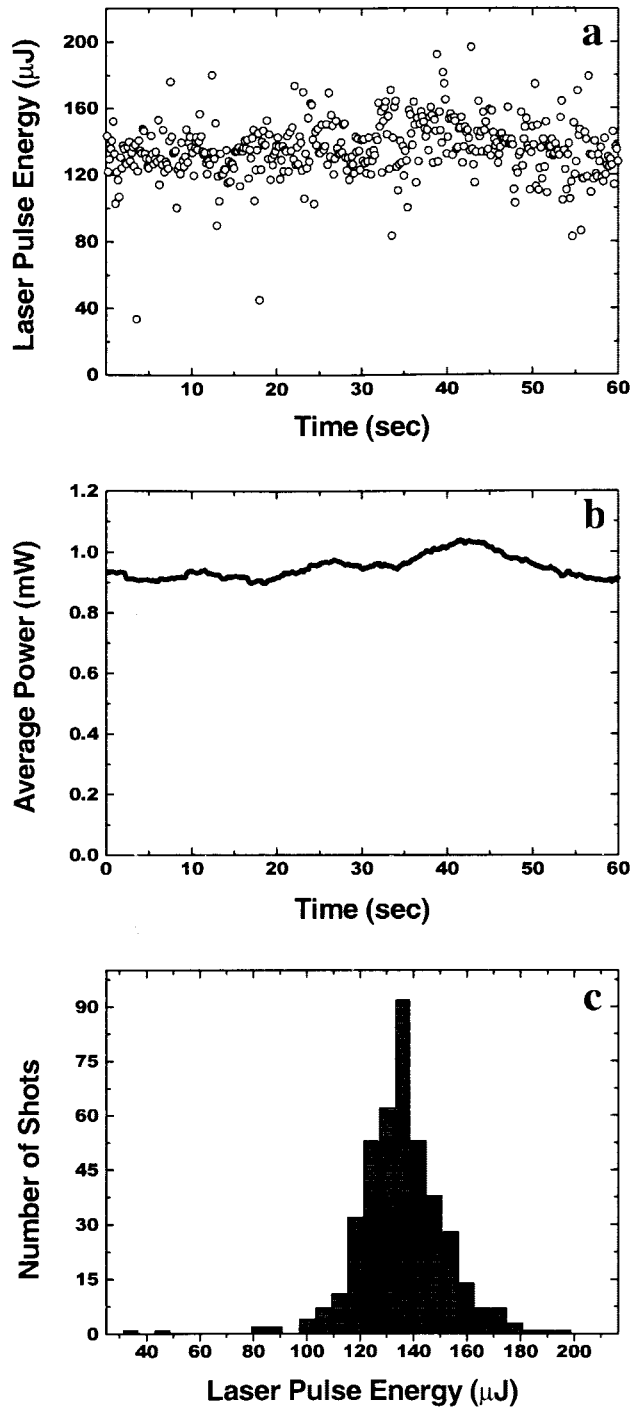


Figure 2.2. Measured output pulse energy and average output power of the 46.9nm laser corresponding to 1 minute of continuous operation at a repetition rate of 7Hz. (a) Shot to shot laser output pulse energy. (b) Average output power computed as a running average of 50 contiguous laser pulses. (c) Distribution of the output pulse energy. The average pulse energy is 135 $\mu\text{J}$  and the standard deviation is 17 $\mu\text{J}$ .

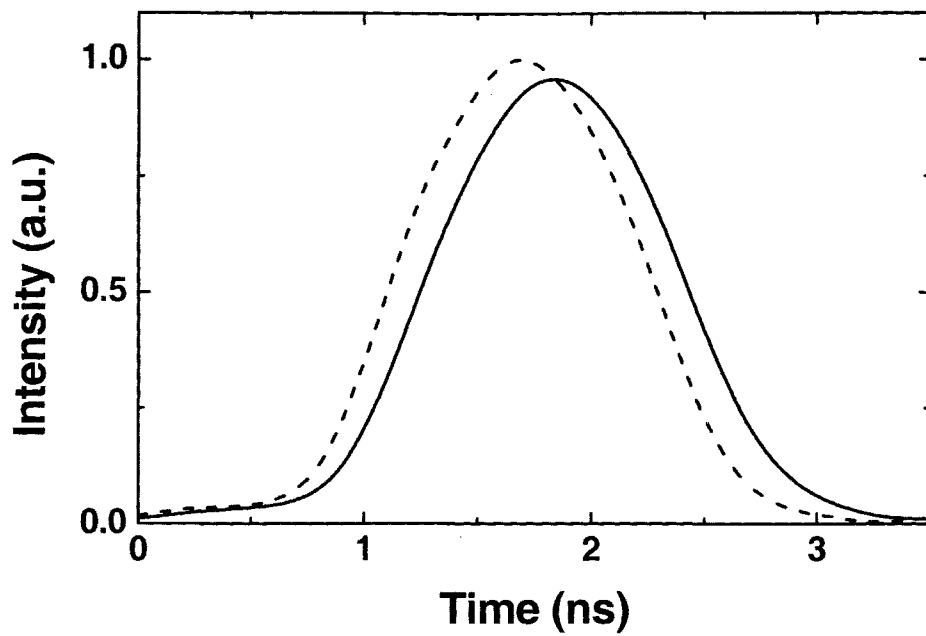


Figure 2.3. Temporal evolution of the laser intensity for a typical laser shot generated at a repetition frequency of 7Hz. The solid curve is the photodiode signal recorded with a 1GHz-bandwidth analog oscilloscope. The dashed curve is the signal corrected for the limited bandwidth of the oscilloscope.

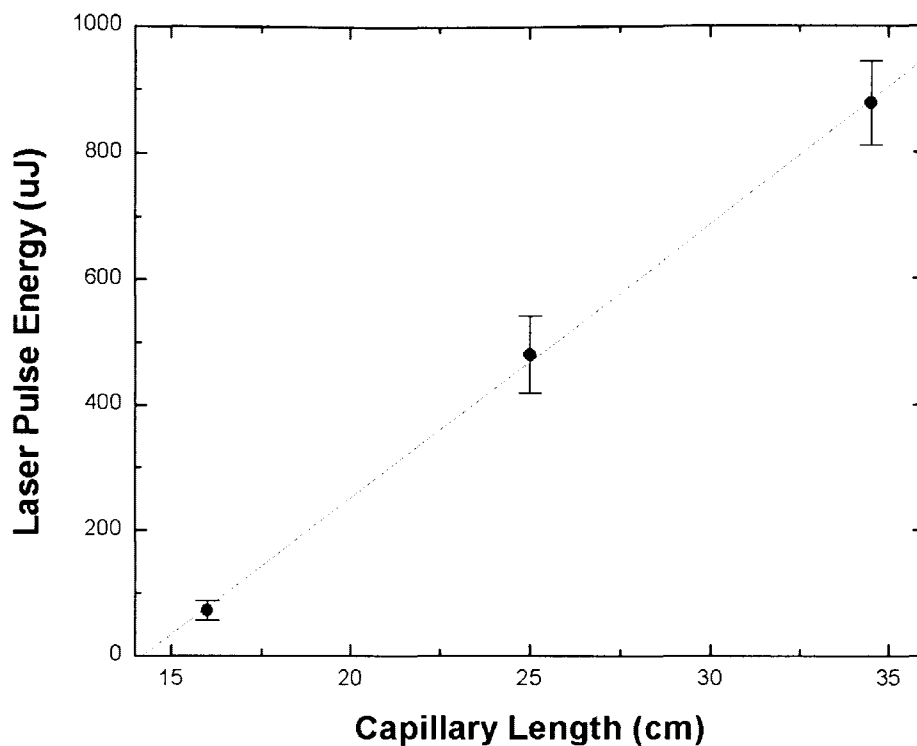


Figure 2.4. Measured average laser output pulse energy as a function of capillary plasma column length. The brackets represent the standard deviation of the shot to shot pulse energy variations corresponding to 400 consecutive laser pulses obtained at a repetition rate of 4 Hz.

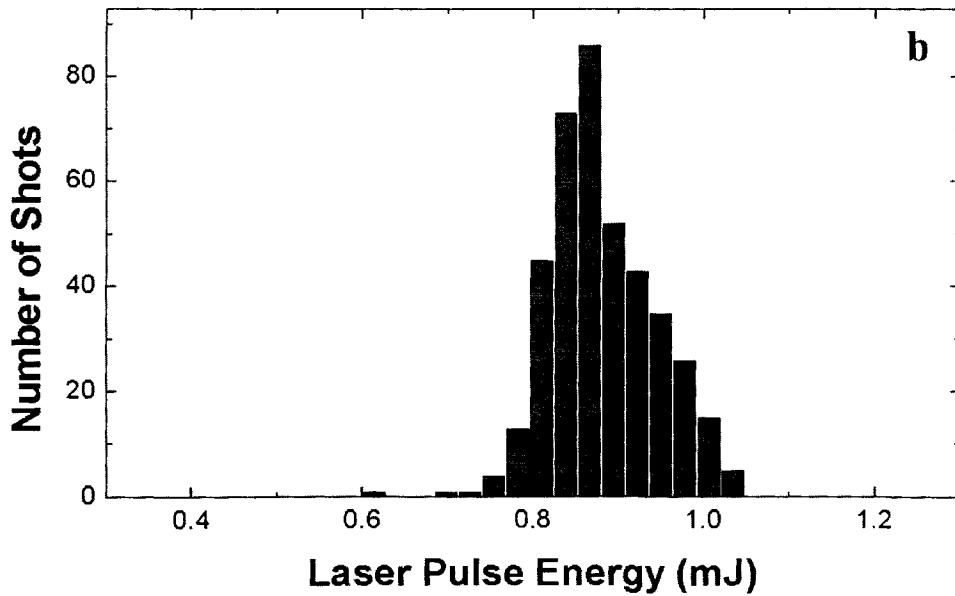
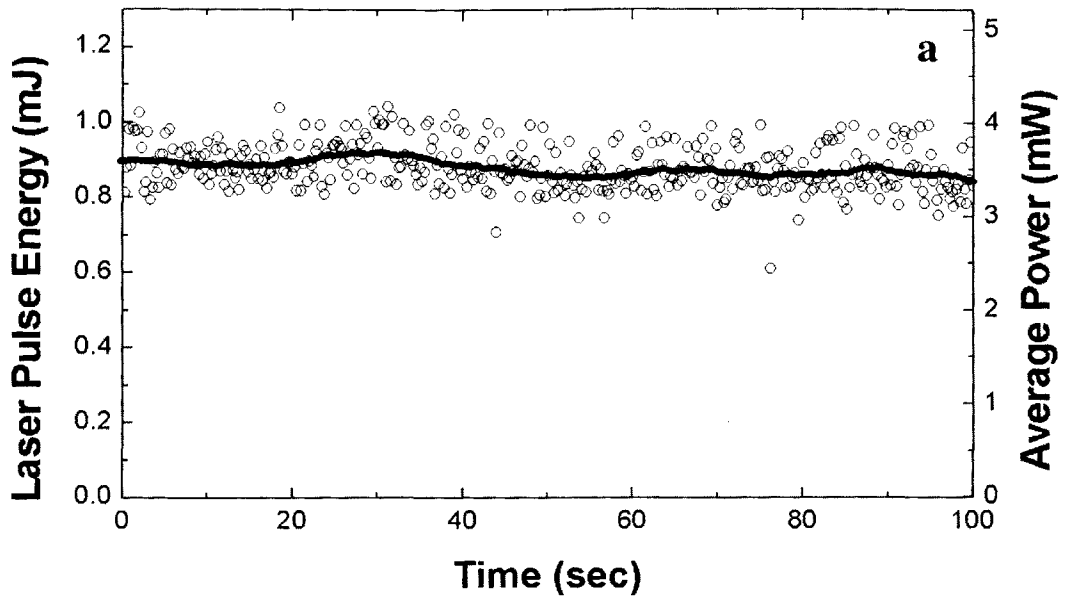


Figure 2.5. Measured laser output pulse energy and average output power corresponding to the 34.5 cm long amplifier operating at a repetition rate of 4 Hz. The data is for 100 seconds of continuous operation of the laser (a) Shot to shot laser output pulse energy. The solid line represents the average output power computed as a walking average of 60 contiguous laser pulses. (b) Distribution of the output pulse energy. The average pulse energy is 0.88 mJ and the standard deviation is  $\pm 0.06$  mJ.

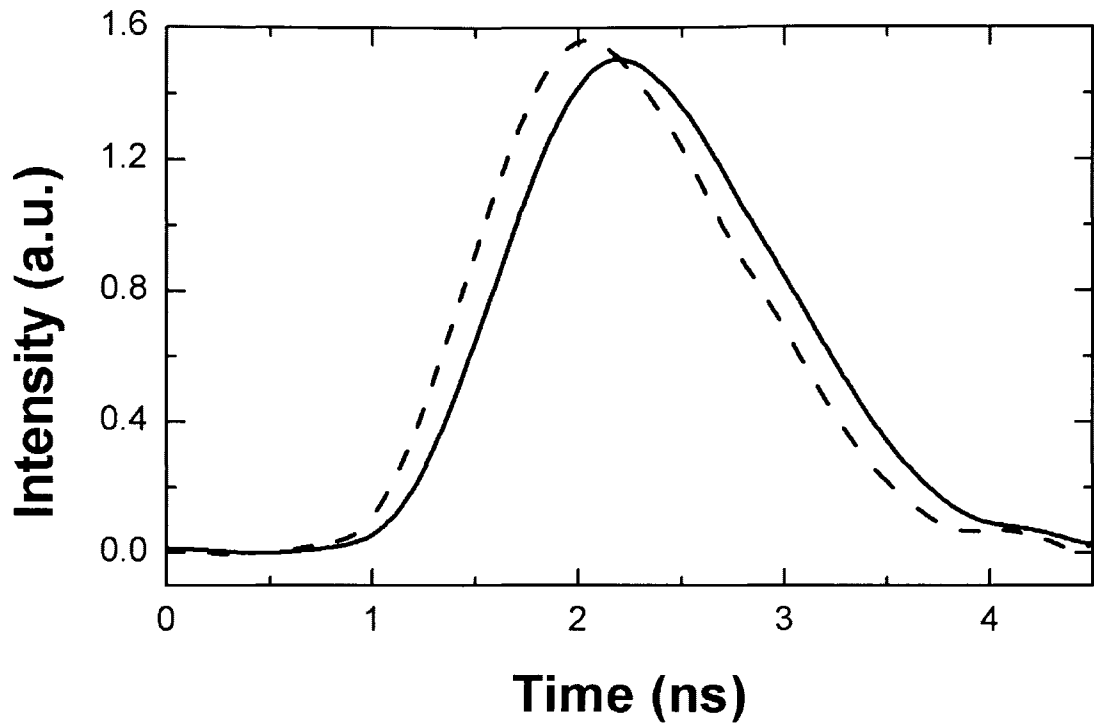


Figure 2.6. Temporal characteristics of the laser pulse corresponding to the 34.5 cm long amplifier. The solid trace is the measured profile. The dashed curve results from correcting the data for the limited bandwidth of the detection system.

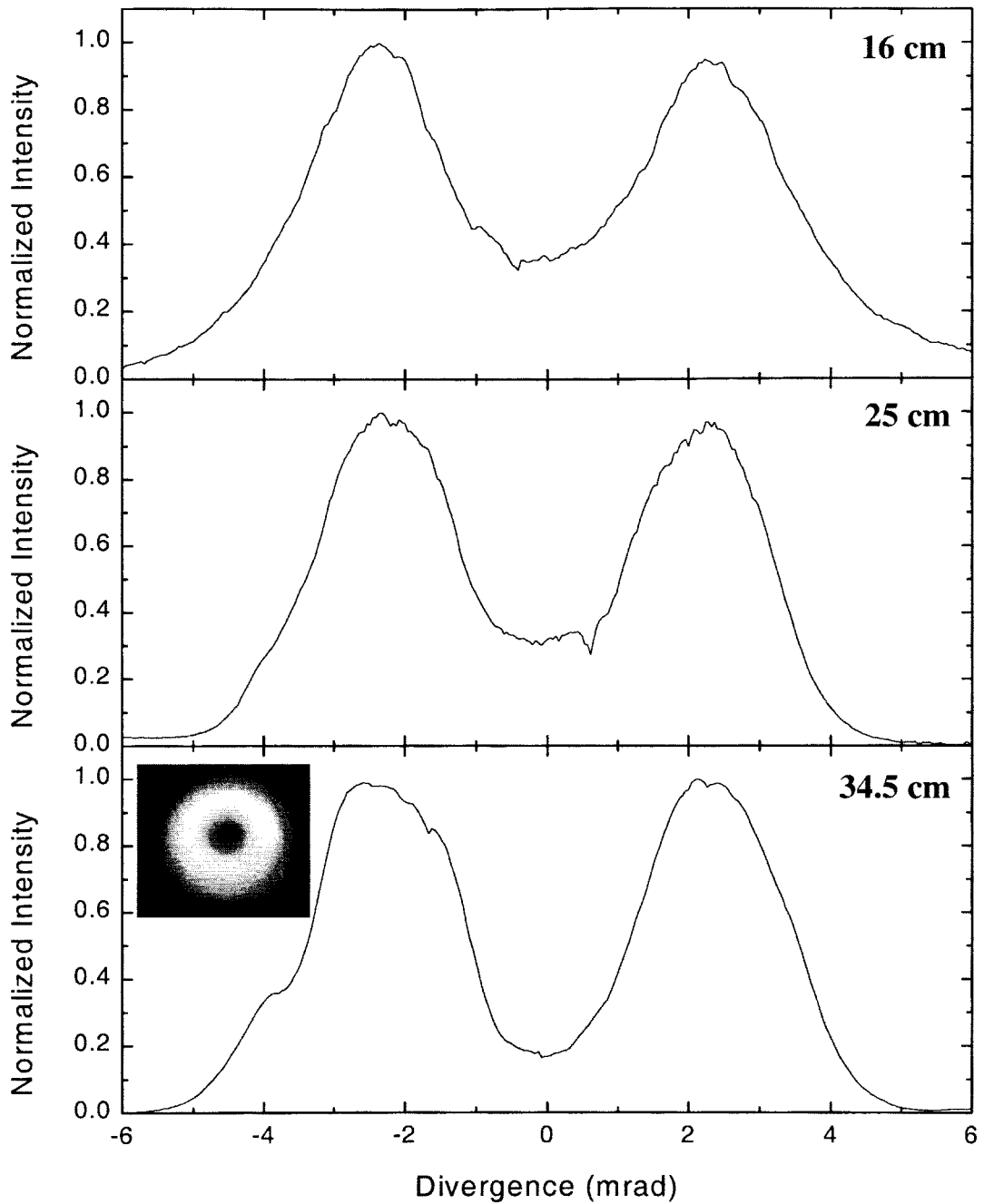


Figure 2.7. Cross sections of the far-field laser intensity distribution patterns corresponding to the different capillary plasma column lengths indicated. The two-dimensional far-field laser intensity distribution pattern for the 34.5 cm long amplifier is shown as an insert.

## 2.9. References

- [2.1] L.B. Da Silva, B.J. MacGowan, S. Mrowka, J. A. Koch, R.A. London, D. L. Matthews and J. H. Underwood, *Opt. Lett.*, 18, 1174 (1993).
- [2.2] P.V. Nickles, V.N. Shlyaptsev, M. Kalashnikov, M. Schnurer, I. Will, and W. Sandner, *Phys. Rev. Lett.*, 78, 2748 (1997).
- [2.3] J. Dunn, A.L. Osterheld, S. Sheperd, W.E. White, V.N. Shlyaptsev, and R.E. Stewards, *Phys. Rev. Lett.*, 80, 2825 (1998).
- [2.4] B.E. Lemoff, G.Y. Yin, C.L. Gordon III, C.P.J. Barty, and S.E. Harris, *Phys. Rev. Lett.*, 74, 1576 (1995).
- [2.5] D. Korobkin, C.H. Nam, S. Suckewer and A. Golstov, *Phys. Rev. Lett.*, 77, 5206 (1996).
- [2.6] D. Korobkin, A. Goltsov, A. Morozov, and S. Suckewer, *Phys. Rev. Lett.* 77, 1476 (1998).
- [2.7] B.R. Benware, C.H. Moreno, D.J. Burd and J.J. Rocca, *Opt. Lett.*, 22, 796 (1997).
- [2.8] J.J. Rocca, V.N. Shlyaptsev, F.G. Tomasel, O.D. Cortazar, D. Hartshorn, and J.L.A. Chilla. *Phys. Rev. Lett.*, 73, 2192 (1994).
- [2.9] J.J. Rocca, D.P. Clark, J.L.A. Chilla and V.N. Shlyaptsev, *Phys. Rev. Lett.*, 77, 1476 (1996).
- [2.10] J.J. Rocca, F.G. Tomasel, M.C. Marconi, V.N. Shlyaptsev, J.L.A. Chilla, B.T. Szapiro and G. Giudice, *Phys. Plasmas*, 2, 2547 (1995).
- [2.11] C.H. Moreno, M.C. Marconi, V.N. Shlyaptsev, B.R. Benware, C.D. Macchietto, J.L.A. Chilla, J.J. Rocca, and A.L. Osterheld, *Phys. Rev. A*, **58**, 1509 (1998).
- [2.12] J.L.A. Chilla and J.J. Rocca. *J. Opt. Soc. Am.* B**13**, 2841, (1996).
- [2.13] T.N. Lee, S. Kim and H. Shin. *SPIE* vol 3156, 250, Ed J.J. Rocca and L.B. Da Silva. (1997).
- [2.14] J. Koch, B.J. MacGowan, L.B. Da Silva, D.L. Mathews, J.H. Underwood, P.J. Batson, and S. Mrowka, *Phys. Rev. Lett.*, 68, 3291 (1992).
- [2.15] M.C. Marconi, J.L.A. Chilla, C.H. Moreno, B.R. Benware, and J.J. Rocca, *Phys. Rev. Lett.*, 79, 2799 (1997).

- [2.16] D.T. Attwood, P. Naulleau, K.A. Goldberg, E. Tejnil, C. Chang, R. Beguiristain, P. Batson, J. Bokor, E.M.Gullikson, H. Medecker, and J.H. Underwood, to be published in IEEE J.Quant.E. (see fig.8, corrected for  $\Delta\lambda/\lambda= 10^{-4}$ ).

## **CHAPTER 3**

### **DETERMINATION OF XUV OPTICAL CONSTANTS BY REFLECTOMETRY USING A HIGH REPETITION RATE 46.9nm LASER**

#### **3.1. Introduction**

The growing interest in the optical properties of solids in the wavelength interval of 35-50 nm is largely stimulated by the advent of compact lasers and high order harmonic sources at these wavelengths [3.1, 3.2, 3.3, 3.4]. Another reason is the development of efficient multilayer optics at these wavelengths [3.5, 3.6] for use in synchrotron radiation research [3.7, 3.8] and astrophysics [3.9]. However, the progress in this area depends significantly on the knowledge of the optical constants of materials within this wavelength range. For some materials, the optical constants at XUV wavelengths have been tabulated [3.10]. However, for many solids the only available data are those from atomic scattering factors [3.11], which ignore the effects of interatomic bonding on the optical spectra. The data show that most of the elements, among them oxygen, nitrogen, carbon and fluorine, are highly absorbing in the interval under consideration. The fact that these materials usually form thin surface contamination layers greatly complicates the accurate measurement of optical constants, especially for the materials with low absorption.

The most popular method for the determination of optical constants is the measurement of normal incidence reflectivity in a wide spectral interval and the application of the Kramers-Kronig relation to calculate both the refractive and absorption indexes [3.12, 3.13]. To do this evaluation one should assume that the reflection of the material is described by the Fresnel formulas. This method results in precise optical constants over the entire wavelength interval, provided the measurement interval is wide enough and the sample surface is free from surface layer impurities. However, most materials develop surface layers of oxide and other impurities when exposed to a natural atmospheric environment. These surface layers can introduce significant errors in the determination of the optical constants for the bulk material.

A second method for the determination of optical constants employs the measurement of angular dependent reflectivity. In this method optical constants at each wavelength can be found by fitting the measured angular dependence of the reflectivity with the Fresnel formula [3.14]. A deviation of the experimental data from the calculated curve for the bulk material is a signal that there is an additional contribution to the reflectivity, which is most likely due to an oxide surface layer. Thus, this method can in principle provide not only optical constants of the bulk material but also information about the surface characteristics of the sample. Moreover, as illustrated herein, when the latter is optically thin, the reflection from the bulk material can be separated from the reflection caused by the surface layer. Therefore, the optical constants of solids can be determined even on partially oxidized or contaminated samples.

Experimental and calculation procedures have been developed in this work for the determination of optical constants at the XUV wavelengths using angular dependent laser

reflectometry. The key device that made the measurements possible is a high repetition rate table-top soft x-ray laser operating at a wavelength of 46.9 nm [3.2]. The laser delivers a beam of 26.5 eV with an average power of up to 1 mW within a spectral bandwidth of  $\lambda/\Delta\lambda > 10^4$ . Section 3.2 describes the experimental setup used in the reflectivity measurements. Section 3.3 discusses the models of a sample's surface used to fit the reflectivity data and gives the details of the data processing. Section 3.4 presents the optical constants for *Si*, *GaP*, *InP*, *GaAs*, *GaAsP* and *Ir*, using the method described herein and gives a comparison with previously published optical constants. Based on these data, the sensitivity of the procedure to the purity of the sample's surface is analyzed. The last section presents the features and prospects for the determination of optical constants in the XUV with the help of ultrashort wavelength lasers.

### **3.2. Experimental setup**

The experimental setup used in the measurements of the reflectance is shown in Figure 3.1. The samples were illuminated with the beam of the Ne-like Ar capillary discharge laser described in chapter 2, operating in a single line at a wavelength of 46.9 nm. For this experiment, the laser was operated at a repetition rate of 1 Hz with capillaries 18.2 cm in length, which yield laser pulses with an energy of approximately 0.1 mJ, and a pulsewidth of  $\cong 1.2$  ns. As detailed in chapter 2, the laser beam divergence was approximately 4.5 mrad.

The measurements were conducted in a vacuum chamber placed at about 1.5 m from the exit of the laser. The samples were mounted on the axis of a rotational stage driven by a stepper motor, which allowed for the selection of angles of incidence between 0 and 90 degrees. The intensity of the reflected beam was recorded with a vacuum

photodiode (labeled “A” in figure 3.1), that was mounted on a lever arm that followed the angular motion of the reflected beam. A 1mm diameter pinhole was placed at the entrance of the chamber to reduce the spot size of the laser beam incident on the sample, which allowed for measurements at grazing angles approaching zero degrees. To overcome scattering of the data due to shot to shot intensity variation of the laser, the intensity of the reflected beam was normalized by the intensity of the incident beam for each laser pulse. For this purpose a reference beam was generated by placing a 50% transmissive gold-plated grid in the path of the incident beam. The intensity of the reference beam reflected by the grid was measured by a second fixed vacuum photodiode (labeled “B” in figure 3.1), and used for the normalization. To obtain absolute reflectance measurements, the signal of the reference photodiode was calibrated with respect to the intensity of the beam transmitted by the grid by removing the sample and positioning the rotating diode in the beam path. This calibration was determined with an error of less than 0.5%. The angular dependence of the reflectivity was measured by scanning the angle of incidence while repetitively firing the laser at a repetition frequency of 1 Hz. The photodiode signals corresponding to the intensity of the reflected beam and reference beams were recorded and stored for every laser shot by a 500 MHz digitizing oscilloscope (Hewlett-Packard model 54825A).

Figure 3.2 is an example of the reflectance data obtained. It shows a single measurement run of the reflectivity as a function of incident angle for a sample of polished crystalline *Si*. This data depicts a typical measurement that consisted of 300 contiguous laser pulses for a 90 degree rotation of the sample. At small angles of incidence, photodiode “A” blocks the beam from impinging on the sample limiting the

minimum angle at which data could be obtained to 1.6 degrees. This angle, which corresponds to the first valid data point near normal incidence, was determined from the geometric dimensions of the system and was used to relate each data point to its corresponding angle. At the other extreme, as the incident angle approaches 90 degrees, the projection of the incident beam on the sample becomes larger than the sample and therefore limited the maximum angle at which valid data could be obtained. In the specific case of the data for the *Si* sample shown in figure 3.2, the 1 mm diameter of the beam limited the measurement to angles less than 85.5 degrees. This accounts for the apparent decrease of the reflectivity at grazing angles that should otherwise approach 100%.

### 3.3. Data analysis

The correct interpretation of measured reflectivity data substantially depends on an adequate model of a sample surface and on the fitting procedure. Three models of the sample surface were investigated to interpret the data. They respectively assume (a) the sample is homogeneous on the scale of light penetration depth, (b) a homogeneous bulk material with a single layer at the surface, (c) a bulk material with two different surface layers.

The first model corresponds to a pure material with complex refractive index  $\tilde{n}_b = n + i \cdot k$  ( $n$  and  $k$  are fitting parameters of the model) with an ideally smooth surface. It results in the reflection that is described by the Fresnel formulas. For an *s*-polarized beam the reflection amplitude is of the form:

$$r_{vb} = \frac{\tilde{n}_v \cos \theta - \tilde{n}_b \cos \theta_b}{\tilde{n}_v \cos \theta + \tilde{n}_b \cos \theta_b} \quad (3.1)$$

where  $\tilde{n}_v = 1$  is the refractive index for vacuum,  $\theta$  is the incident angle and  $\theta_b$  is given by Snell's law:  $\tilde{n}_v \sin \theta = \tilde{n}_b \sin \theta_b$ . For a beam with  $p$ -polarization the only change is the substitution of  $1/\tilde{n}$  for  $\tilde{n}$  in  $r_{vb}$ .

The second model assumes a sample with a single homogeneous layer at the surface, which has an ideally sharp permittivity profile and smooth interface with the bulk material. The model has five parameters: the complex refractive indexes for the surface layer  $\tilde{n}_l$  and bulk material  $\tilde{n}_b$ , and the layer thickness  $d_l$ . For this model the reflection amplitude is given by the expression:

$$r = \frac{r_{vb} + r_{lb} \exp(2iD)}{1 + r_{vl} r_{lb} \exp(2iD)} \quad (3.2)$$

where  $D = n_l \cos \theta (2\pi d_l / \lambda)$ , and  $r_{vl}$ ,  $r_{lb}$  are the reflection amplitudes at the interfaces: vacuum–surface layer and surface layer–bulk material, correspondingly. These amplitudes are described by equations similar to Equation 3.1.

The third model imitates a gradual decrease of oxidization from the surface to the bulk material. It contains eight parameters: the complex refractive indexes for the first layer  $\tilde{n}_{l1}$ , the second layer  $\tilde{n}_{l2}$ , the bulk material  $\tilde{n}_b$  and the thickness of each layer  $d_{l1}$  and  $d_{l2}$ . In this case, the magnitude of the reflection can again be put in the form of Equation 3.2 with the substitution of  $r_{vl1}$  for  $r_{vl2}$  and  $r_{l1l2}$  for  $r_{lb}$ , where  $r_{l1l2}$  is the reflection amplitude at the interface between the first and second layers.

Note that all three models ignore microroughness of the surface and the interfaces. It is known that microroughness mainly redistributes reflected light between specular reflection and diffuse scattering. The aperture of our detector was 8.8 mm in diameter and sustained an angle of 44 mrad with respect to the beam spot on the sample.

Estimation of scattering effects shows that for a roughness correlation length greater than 14  $\mu\text{m}$  the majority of the scattered radiation was registered by the detector, even at grazing angles. For higher spatial frequency roughness the grazing angle scattering was evaluated to be negligible if the RMS roughness height is less than 0.5  $\mu\text{m}$ . For this reason the effect of microroughness was not taken into account in our calculations. A detailed discussion of this problem can be found in [3.15].

The fitting of the model parameters was carried out by the standard least-squares method using the following merit function  $F$ :

$$F = \frac{1}{N} \sum_{i=1}^N ((R_{\text{exp}}(\theta_i) - R_{\text{th}}(\theta_i)) / R_{\text{exp}}(\theta_i))^2 \quad (3.3)$$

where  $R_{\text{exp}}(\theta_i)$  and  $R_{\text{th}}(\theta_i)$  are the measured and calculated reflectivities at the incident angle  $\theta_i$ , and  $N$  is the number of angles at which measurements were obtained. Since the measurements were carried out with unpolarized light the calculated reflectivity was averaged over the two polarizations, that is  $R_{\text{th}} = (R_{\text{th}}^s + R_{\text{th}}^p)/2$ . One can see that the function  $F$  is written in the form of the squared relative RMS error of the fitting.

To judge the validity of the model, the obtained minimum of  $F$  should be compared with the relative RMS error of the experiments, which can be estimated as:

$$\langle \Delta R / R \rangle = \sqrt{\frac{1}{N} \sum_{i=1}^N ((R_{\text{exp}}(\theta_i) - \langle R_{\text{exp}}(\theta_i) \rangle) / \langle R_{\text{exp}}(\theta_i) \rangle)^2} \quad (3.4)$$

where  $\langle R_{\text{exp}}(\theta_i) \rangle$  is the smoothed experimental angular dependent reflectivity. Assuming that the true reflectivity should not oscillate inside the interval of  $\Delta\theta \sim 5$  degrees, we smoothed the measured reflectivity by the least squares fitting to a quadratic polynomial in  $\theta$  over  $\Delta\theta$ .

The calculations showed that the second model minimizes the merit function  $F$  much better than the first. However, the third model only slightly decreases the minimum of  $F$  in comparison with the single layer model, and the difference between the merit functions was much less than  $\langle \Delta R/R \rangle^2$ . In other words, the reflectivity was demonstrated to be dependent on the optical thickness of the surface layer, but rather insensitive to its spatial distribution. Since it is not necessary to consider a spatially distributed surface layer, the third model was excluded and the final calculations of optical constants described in the next section are based only on the first and the second models. The fitting parameters were found by minimization of the merit function  $F$  up to convergence using a quasi-Newton method. The local minimum of  $F$  with the correspondent values of the optical constants can then be found using this technique [3.16]. The typical time of the computations was 2-4 s for the first model and 10-30 s for the second model (Pentium II 233 Mhz class computer).

### **3.4. Results of the determination of optical constants**

Measurements of the dependence of the reflectivity on the angle of incidence were performed using the setup described in section 3.2. To decrease random experimental errors, several runs of measurements were usually carried out and the results were averaged to produce one reflectivity curve. From the experimental reflectivity dependence such as that shown in figure 3.2 the range of validity for the data was chosen to be  $1.8^\circ < \theta < 85^\circ$  (affected by the sample's size), which usually consisted of 270-350 data points.

All the semiconductor samples were bulk crystalline with a 100 orientation with the exception of the GaAsP, which was an epitaxial layer grown on a GaAs wafer of 100

orientation. The Si sample was P type with B dopant at a carrier concentration of  $5 \times 10^{17} \text{ cm}^{-3}$ . The GaP was P type with Zn dopant at a carrier concentration of  $1.2 \times 10^{18} \text{ cm}^{-3}$ . The InP was N type with S dopant at a carrier concentration of  $1 \times 10^{18} \text{ cm}^{-3}$ . The GaAs was P type with Zn dopant at a carrier concentration of  $1.2 \times 10^{19} \text{ cm}^{-3}$ . The GaAsP sample was a thick epitaxially grown layer of  $\text{GaAs}_{0.6}\text{P}_{0.4}$  on a GaAs substrate. Due to the strain from a lattice mismatch between the epitaxial layer and the substrate, this sample exhibited periodic surface structure. However, the RMS roughness of this structure was measured to be less than  $0.5 \text{ }\mu\text{m}$ . The Ir was electron beam evaporated as a thick film onto a super polished (RMS surface roughness  $\approx 1 \text{ }\text{\AA}$ ) glass substrate.

In order to more fully characterize the influence of the surface layer on the measurements, the samples of Si, GaP and InP were chemically treated in the following manner to alter the characteristics of the surface layer. The samples were dipped in a 5% solution of HF in distilled water for approximately 5 minutes and were then rinsed with acetone and methanol. The samples were exposed to ambient atmospheric conditions for less than 5 minutes before being positioned in the system under a vacuum of about  $1 \times 10^{-5}$  torr. In the case of the Si, the measured reflectivity for a treated sample was significantly different from that of an untreated sample. However, the reflectivity curve of the treated sample did not appreciably change after exposure to the ambient environment for more than 12 hours. This suggests, and it has been previously shown that this chemical treatment passivates the Si surface and prevents further oxide growth [3.17].

The results of fitting the data for each sample with the two models are shown in figures 3.3-3.8. As an example, first consider the data processing technique and evaluation of the optical constants for the Si sample shown in figure 3.3. This figure

shows the measured reflectivity of an untreated *Si* sample as well as the corresponding results of the least-squares fit. The dotted and solid curves  $R(\theta)$  were calculated with the first and the second models respectively (Equations 3.1 and 3.2 for the reflection amplitudes). As illustrated in figure 3.3, the shape of the measured reflectivity dependence cannot be fit without assuming the existence of a surface layer. The curve seems to consist of two parts with a kink around  $\theta \approx 58^\circ$ . Despite the fact that each of these parts may be fit by the Fresnel formula (Equation 3.1) it is not possible to obtain a good fit for the entire data set utilizing the first model. However, the second model allows for the fitting of such curves. This fact emphasizes the need to measure the reflectivity over all the angular range including near normal incidence angles where the reflectivity is low. The high intensity of the laser source is an advantage for the accurate measurements of the reflectivity at near-normal incidence, where the reflectivity of most materials is low.

In general the second model provides a much better approximation to the experimental data for all the data obtained. This results in smaller minimum values of the merit function. For example, fitting the data corresponding to the untreated *Si* sample gives  $F_1 = 6 \cdot 10^{-2}$  and  $F_2 = 5 \cdot 10^{-3}$  for the first and second models respectively. In addition, note that the minimum of  $F_2$  is of the order of the experimental RMS error  $\langle \Delta R/R \rangle^2 = 2 \cdot 10^{-3}$ . It is not surprising that optical constants  $n$  and  $k$  evaluated in the frames of these two models are different:  $n = 0.844$  and  $k = 0.023$  for the first and :  $n = 0.817$  and  $k = 0.015$  for the second model. Note that in minimizing  $F$  we used permittivities  $\epsilon_1 = n^2 - k^2$  and  $\epsilon_2 = 2nk$  as fitting parameters. Though our method is not intended for the accurate determination of the optical constants for the surface layer, the obtained parameters  $d_l =$

1.8 nm,  $n_l = 0.75$  and  $k_l = 0.29$  are in this case close to those of a typical layer of  $SiO_2$  commonly found on the surface of  $Si$ :  $d=2-3$  nm,  $n = 0.82$  and  $k = 0.23$  [3.10]. However, as shown below this is not always the case.

The measured reflectivity of a treated sample of  $Si$  is presented in figure 3.3b. The measurement was carried out in one run; therefore the scattering of data is larger than in figure 3.3a. One can observe significant changes in the shape of the angular dependence: the reflectivity is closer to one at grazing angles and the break is smoother. Again, the second model gives a much better description of the experimental dependence. The resulting optical constants of bulk  $Si$  are now:  $n = 0.800$  and  $k=0.02$ , that is, are only slightly different from those of the same sample of  $Si$  before it was chemically treated. This consistency between the results for treated and untreated samples, which was also found for  $GaP$  and  $InP$ , provides evidence of the good accuracy of the method for the determination of optical constants of bulk materials. On the other hand, the best fit to the data of the chemically treated  $Si$  sample gives a rather uncharacteristic value of 9.3 nm for the thickness of the surface layer. This is an indication that the method is not adequate for the accurate determination of the surface layer parameters.

Figures 3.4-3.7 illustrate the measured reflectivity curves for several other semiconductor materials:  $GaP$ ,  $InP$ ,  $GaAs$ ,  $GaAsP$ . All these data show general features similar to that of  $Si$  although, due to higher absorption of these materials, the effects of the absorptive surface layer are less noticeable. For the case of the  $Ir$  film (figure 3.8) in which the absorption for the bulk material is the highest, a kink on the angular dependence is not seen and both models give very similar results. Nevertheless, introducing a single surface layer (the second model) leads to a better fit and an

improvement in the value of the merit function by several times.

The determined optical constants for the materials that were investigated are collected in Table 3.1 along with the available constants from a handbook [3.10]. The

No	Sample	Treated	This work		Ref.[3.10]	
			n	k	n	k
1	<b>Si</b>	<b>No</b>	0.82	0.015	0.803	0.0178
2		<b>Yes</b>	0.80	0.021		
3	<b>GaP</b>	<b>No</b>	0.82	0.052	N/A	0.100
4		<b>Yes</b>	0.82	0.055		
5	<b>InP</b>	<b>No</b>	0.88	0.087	N/A	N/A
6		<b>Yes</b>	0.89	0.090		
7	<b>GaAs</b>	<b>No</b>	0.84	0.060	N/A	0.083
8	<b>GaAsP</b>	<b>No</b>	0.83	0.059		
9	<b>Ir</b>	<b>No</b>	0.81	0.53	0.67	0.69

Table 3.1. Optical constants measured in this work compiled with those of previous work in [3.10].

table shows that the values obtained in this work are rather close to those previously reported [3.10], however, the absorption indexes are lower than those tabulated in the handbook. This discrepancy may arise from a difference of the chemical and physical properties of the particular samples. While the samples studied were mostly commercially available bulk crystalline, the referenced data [3.10] were obtained for specially prepared materials usually deposited as a thin layer. As was noted in [3.10], optical constants in UV and XUV spectral range critically depends not only on the chemical composition of the samples but also on a number of technological factors: the temperature of deposition, speed of deposition, vacuum conditions, etc. For example, in the case of Si (deposited as a thin film), handbook [3.10] gives two values for n and k obtained for two different samples by two different groups of authors. The two values of the absorption coefficient k differ by about 400%. This example indicates the strong

dependency of the optical properties of the samples on particular chemical and physical conditions of manufacturing.

### 3.5. Conclusion

Optical constants at a wavelength of 46.9nm were determined for *Si*, *InP*, *GaP*, *GaAs*, *GaAsP* and *Ir* utilizing the high repetition rate table-top laser discussed in chapter two. The high intensity of the laser source is an advantage for the accurate measurements of the reflectivity at near-normal incidence, where the reflectivity of most materials is low. The measurements for *InP* and *GaAsP* constitute the first experimental values at this wavelength while the rest are in most cases relatively close to those previously tabulated. An important feature of this wavelength region is the very high sensitivity of reflectance to the presence of organic and inorganic compounds, which contaminate the surface of the sample in natural environment conditions. Therefore to obtain accurate values of optical constants using reflectometry, it is important to consider both the reflection from the bulk material as well as the reflection from the contaminated surface layer. The analysis of the data made use of models that take into account the presence of a surface layer of contaminants. Comparison of the values of the optical constants obtained from having surface layers of different characteristics shows that the optical constants of the bulk material obtained with this treatment remain unchanged even when the characteristics of the surface layer changes significantly. This suggests that the approach used in this work might be capable of improving the determination of optical constants, which is important for the design and construction of improved normal incidence reflective coatings for optical devices operating in the XUV. For further work, the separate use of *s*- and *p*- polarized beams for reflectivity measurements also looks

promising as it gives useful additional information. The experiment reported herein constitutes the first application of a soft x-ray laser to materials research. These measurements demonstrate that compact high repetition rate soft x-ray lasers can provide an attractive table-top alternative to synchrotron sources for certain material science problems.

### 3.6. Figures

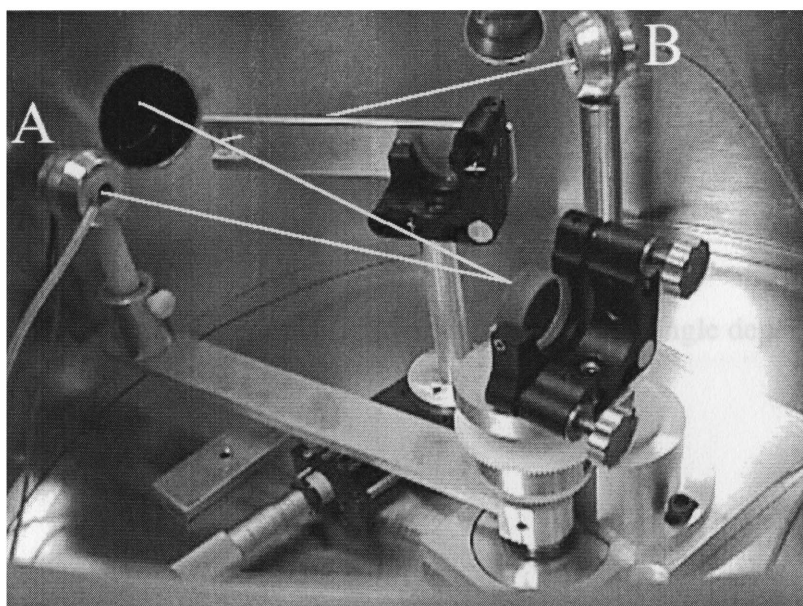
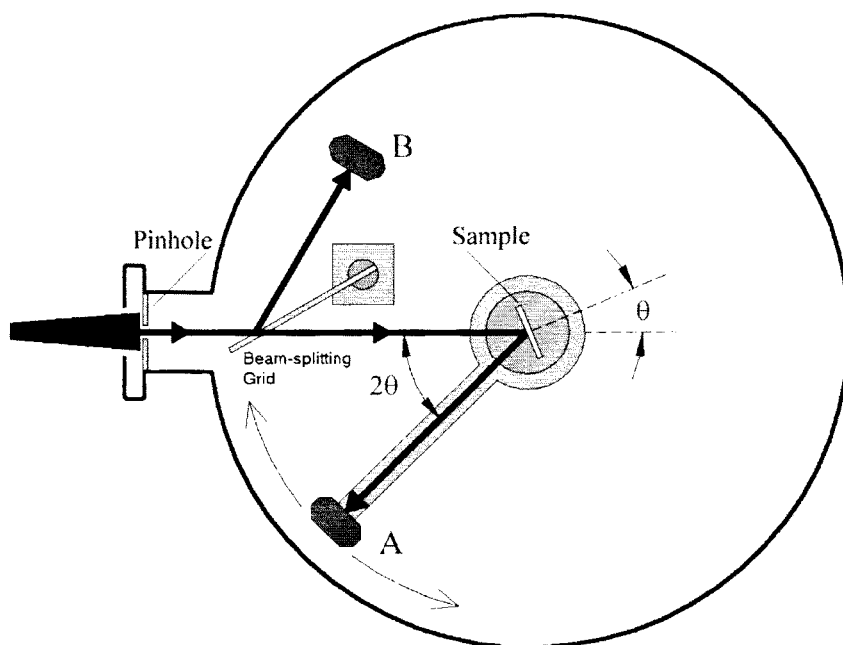


Figure 3.1. Schematic diagram and photograph of the laser reflectometer used in the measurement of XUV optical constants.

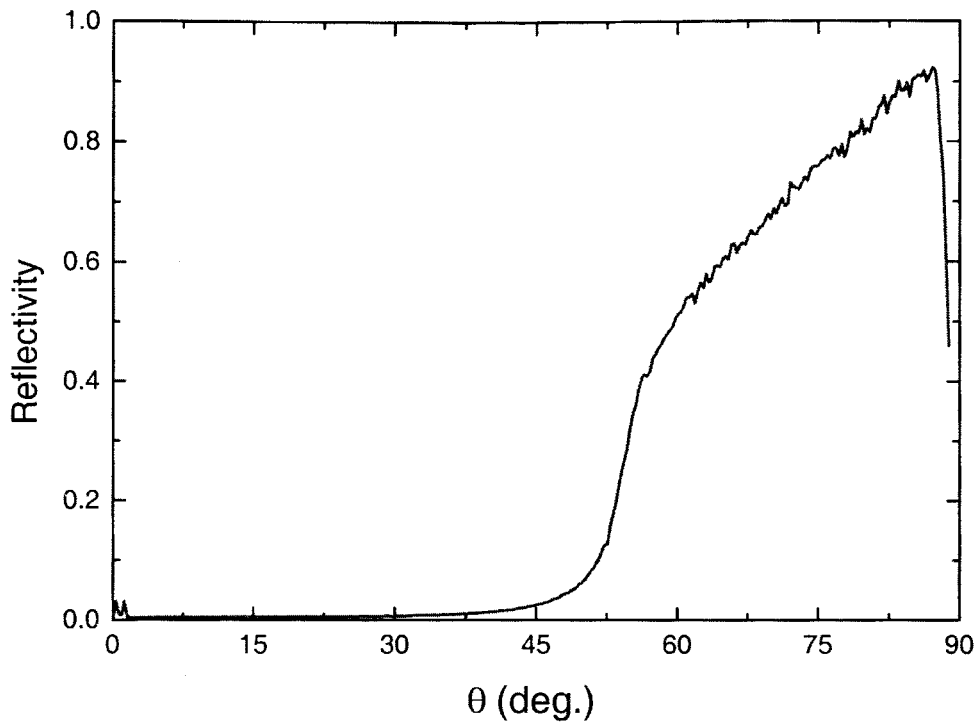


Figure 3.2. Example of measured reflectivity vs incident angle dependence in the range  $0^\circ < \theta < 90^\circ$  for a *Si* sample.

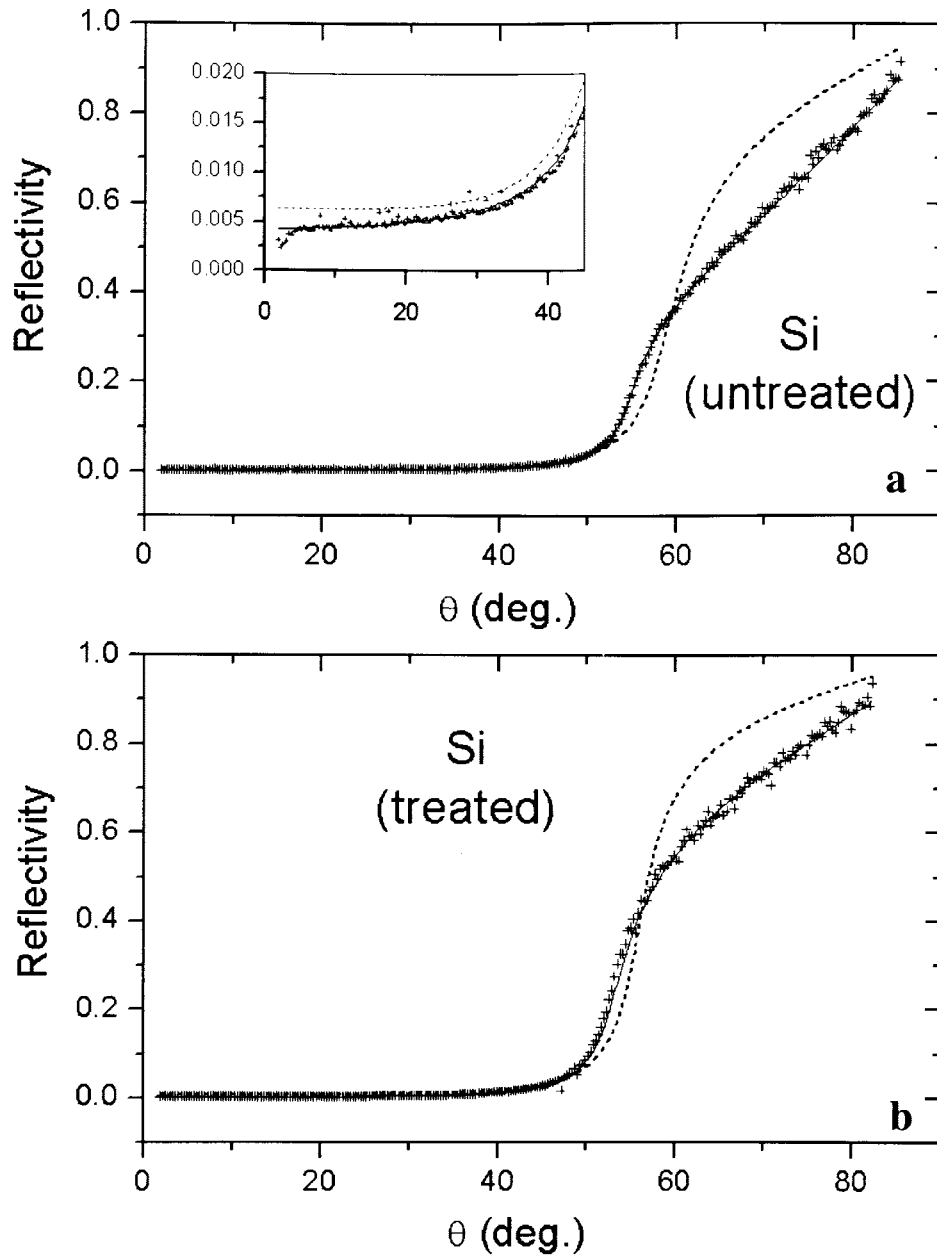


Figure 3.3. Measured and calculated reflectivity for a 100 crystalline *Si* sample as function of the incident angle  $\theta$ . **(a)** Before chemical treatment. The dotted curve is calculated with the optimal optical constants  $\tilde{n}_b = 0.85 + i \cdot 0.023$  without a surface layer (the first model). The solid curve was obtained in the frame of the second model with the optimal parameters for  $\tilde{n}_b = 0.82 + i \cdot 0.015$  and surface layer parameters:  $\tilde{n}_l = 0.75 + i \cdot 0.30$ , thickness  $d_l = 1.8$  nm; **(b)** After chemical treatment. The dotted curve corresponds to parameters:  $\tilde{n}_b = 0.85 + i \cdot 0.023$  without the surface layer, the solid curve:  $\tilde{n}_b = 0.80 + i \cdot 0.021$  (layer:  $\tilde{n}_l = 0.94 + i \cdot 0.021$ , thickness  $d_l = 9.3$  nm).

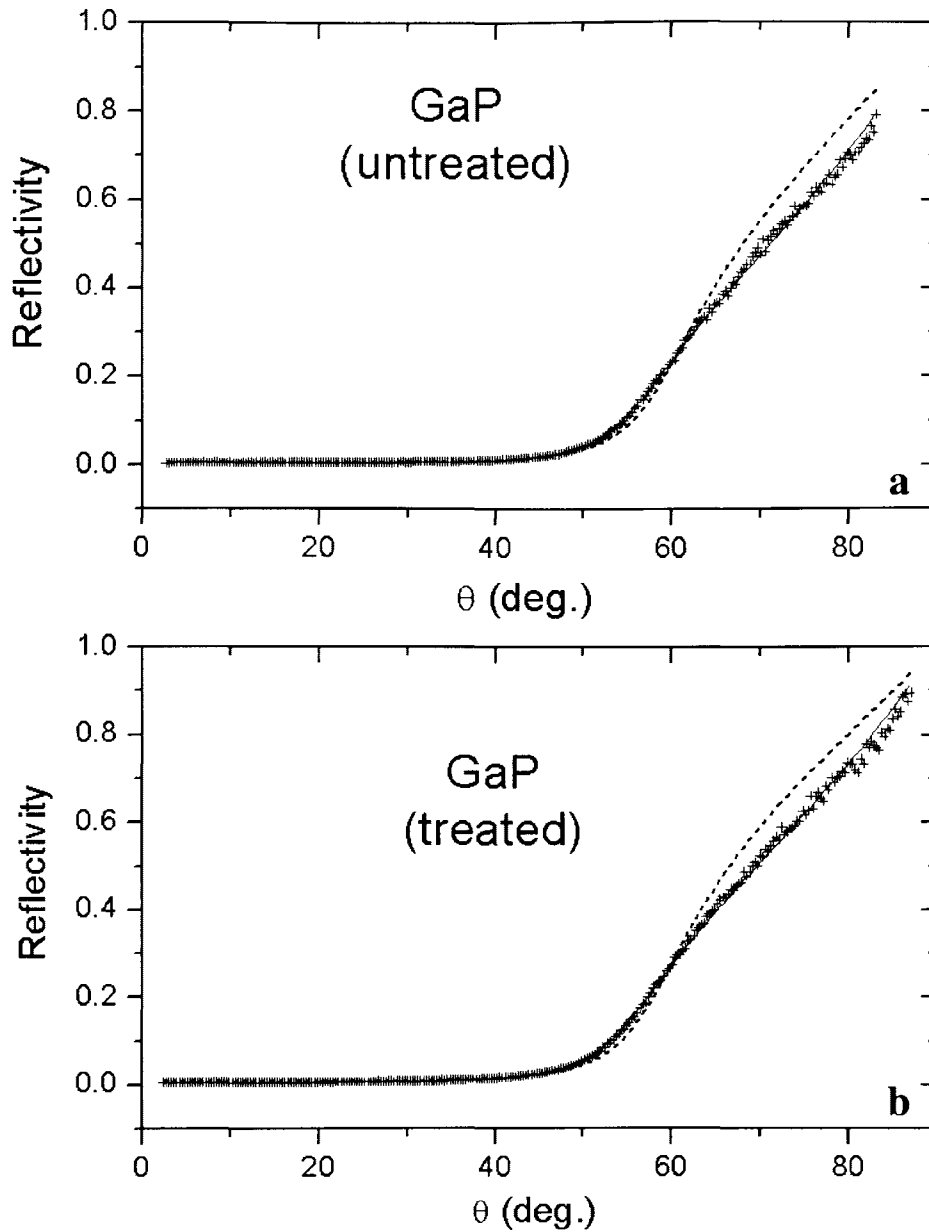


Figure 3.4. Measured and calculated reflectivity for 100 crystalline *GaP* as function of the incident angle  $\theta$ . **(a)** Before chemical treatment. The dotted curve corresponds to:  $\tilde{n}_b = 0.86 + i \cdot 0.050$  without the surface layer, the solid curve:  $\tilde{n}_b = 0.82 + i \cdot 0.052$  ( layer:  $\tilde{n}_l = 0.78 + i \cdot 0.44$ , thickness  $d_l = 0.98$  nm). **(b)** After chemical treatment. The dotted curve corresponds to:  $\tilde{n}_b = 0.85 + i \cdot 0.048$  without the surface layer, the solid curve:  $\tilde{n}_b = 0.82 + i \cdot 0.055$  ( layer:  $\tilde{n}_l = 0.82 + i \cdot 0.32$ , thickness  $d_l = 1.1$  nm).

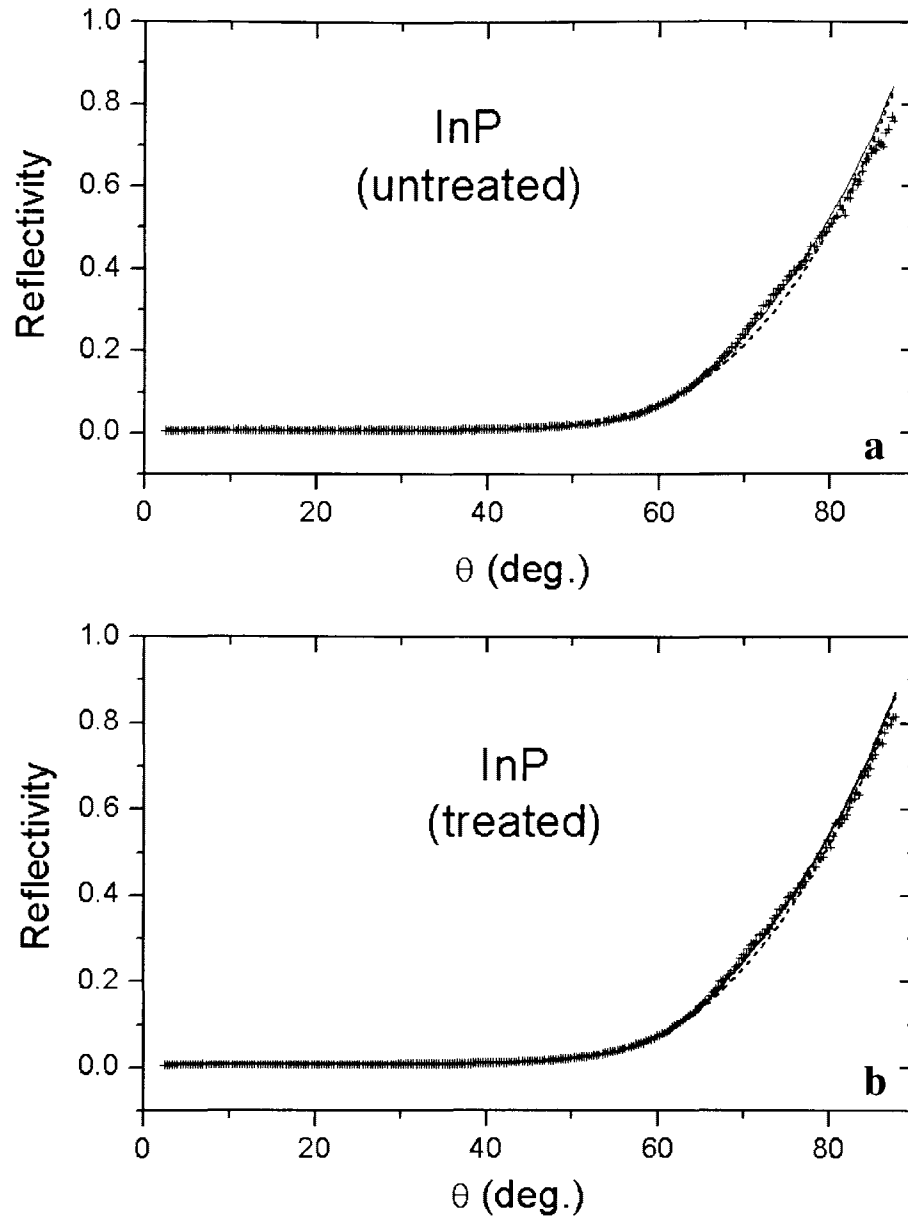


Figure 3.5. Measured and calculated reflectivity for 100 crystalline *InP* as function of the incident angle  $\theta$ . (a) Before chemical treatment. The dotted curve corresponds to:  $\tilde{n}_b = 0.92 + i \cdot 0.14$  without the surface layer, the solid curve:  $\tilde{n}_b = 0.88 + i \cdot 0.087$  ( layer:  $\tilde{n}_l = 0.82 + i \cdot 0.39$ , thickness  $d_l = 1.8$  nm); (b) After chemical treatment. The dotted curve corresponds:  $\tilde{n}_b = 0.91 + i \cdot 0.13$  without the surface layer, the solid curve:  $\tilde{n}_b = 0.88 + i \cdot 0.09$  ( layer:  $\tilde{n}_l = 0.84 + i \cdot 0.26$ , thickness  $d_l = 2.5$  nm).

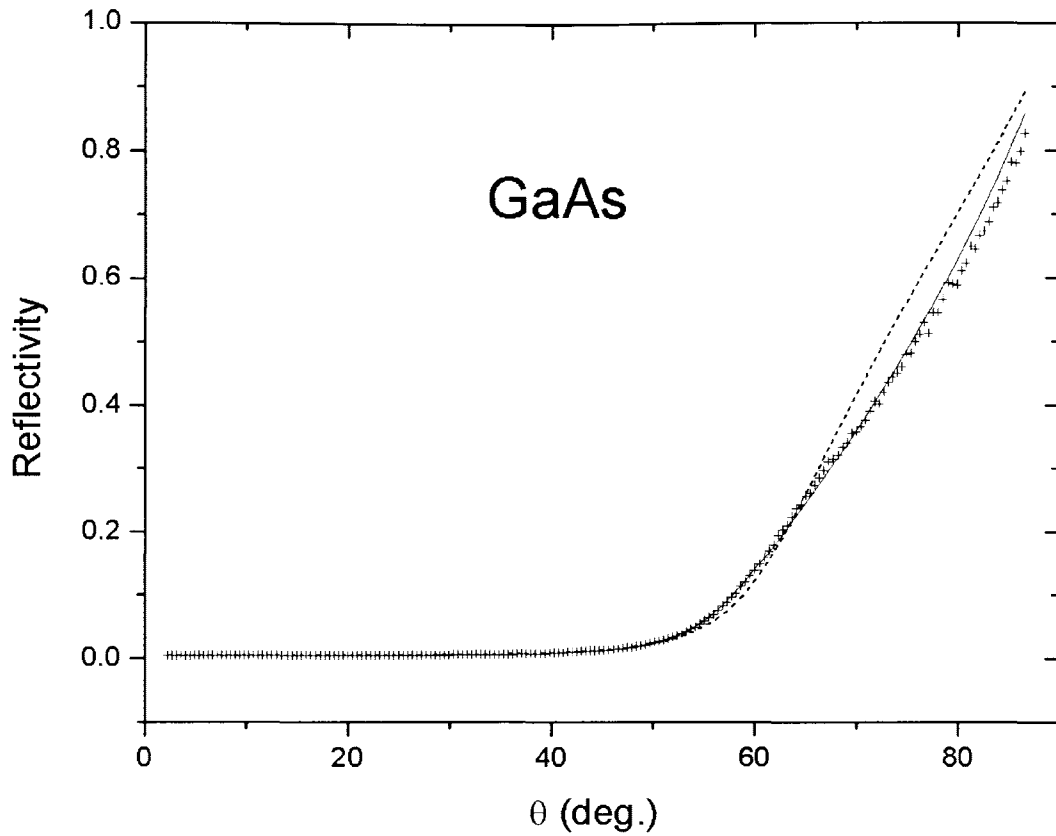


Figure 3.6. Measured and calculated reflectivity for 100 crystalline *GaAs* as function of the incident angle  $\theta$ . The dotted curve corresponds to:  $\bar{n}_b = 0.88 + i \cdot 0.058$  without the surface layer, the solid curve:  $\bar{n}_b = 0.84 + i \cdot 0.06$  (layer:  $\bar{n}_l = 0.84 + i \cdot 0.30$ , thickness  $d_l = 2.4$  nm).

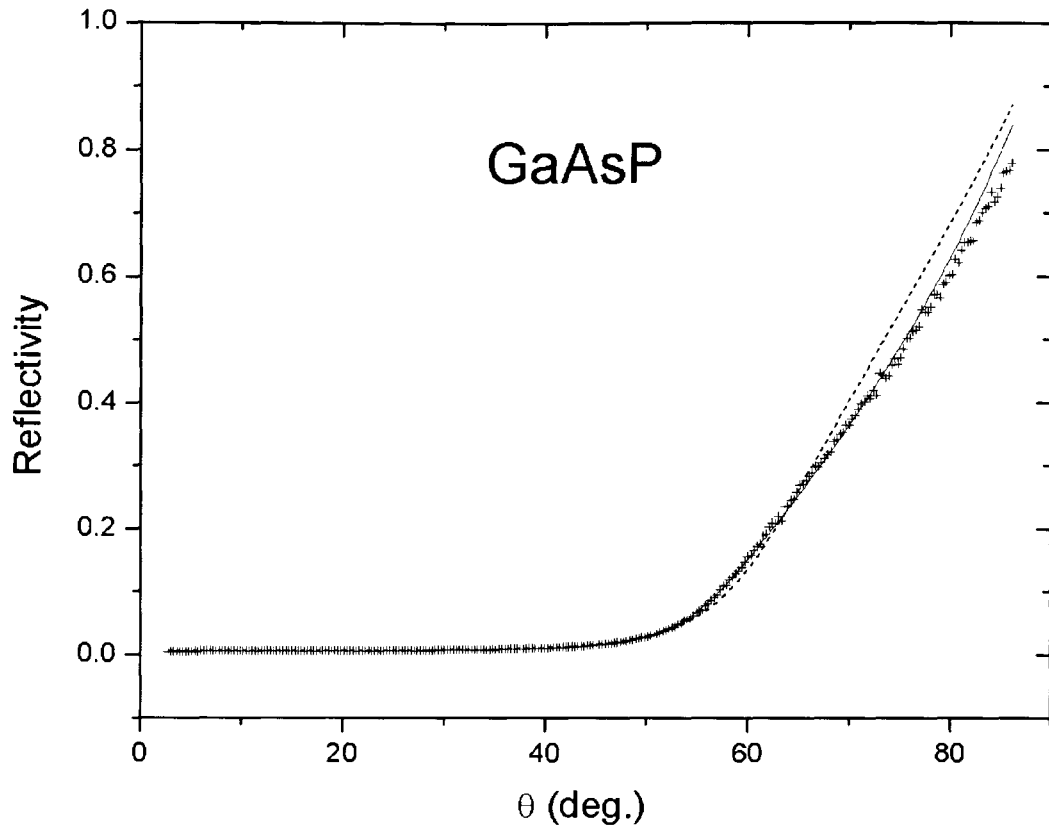


Figure 3.7. Measured and calculated reflectivity for a thick epitaxial film of *GaAsP* as function of the incident angle  $\theta$ . The dotted curve corresponds to:  $\tilde{n}_b = 0.88 + i \cdot 0.07$  without the surface layer, solid curve:  $\tilde{n}_b = 0.83 + i \cdot 0.059$  (layer:  $\tilde{n}_l = 0.81 + i \cdot 0.39$ , thickness  $d_l = 2.0$  nm).

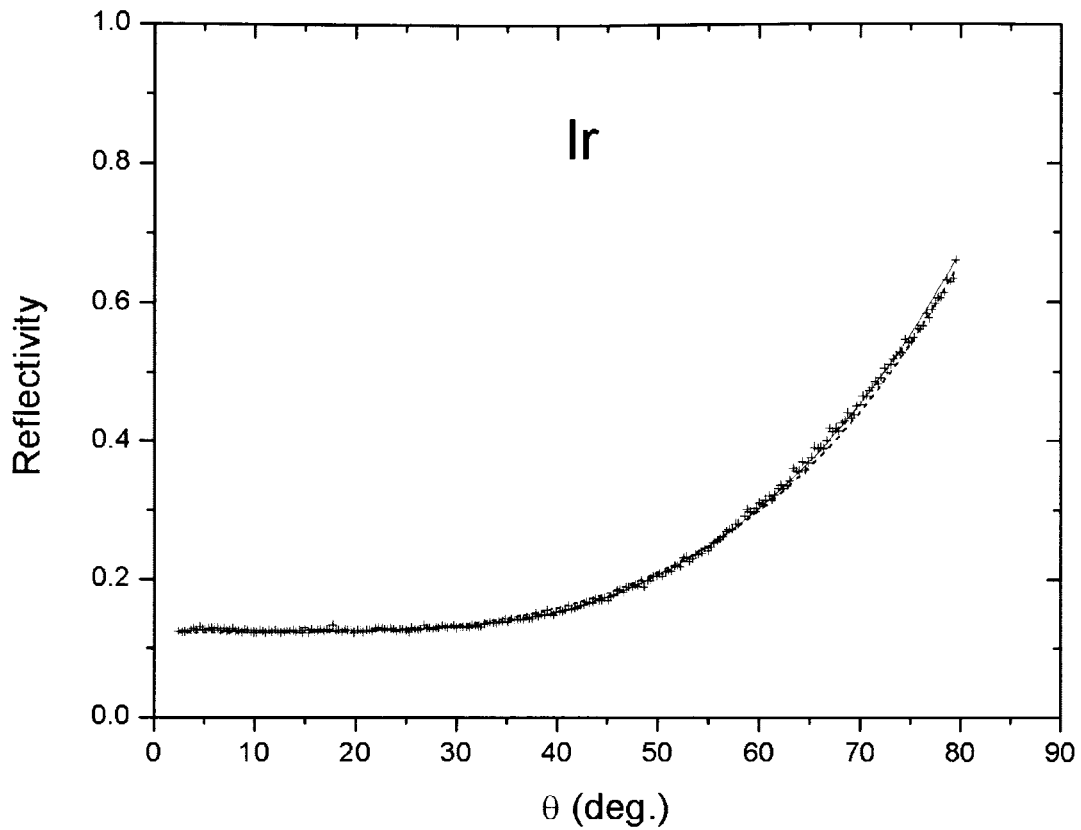


Figure 3.8. Measured and calculated reflectivity for an electron beam evaporated *Ir* film as a function of the incident angle  $\theta$ . The dotted curve corresponds to:  $\tilde{n}_b = 0.76 + i \cdot 0.60$  without the surface layer, the solid curve:  $\tilde{n}_b = 0.81 + i \cdot 0.53$  (layer:  $\tilde{n}_l = 0.83 + i \cdot 0.006$ , thickness  $d_l = 3.7$  nm).

### 3.7. References

- [3.1] J.J.Rocca, V.N.Shlyaptsev, F.G.Tomasel, O.D.Cortazar, D.Hartshom, and J.L.A.Chilla, *Phys. Rev. Lett.*, vol.73, pp. 2192–2195, 1994.
- [3.2] B.R. Benware, C.D. Macchietto, C.H. Moreno, and J.J. Rocca, *Phys. Rev. Lett.*, vol. 81, pp. 5804-5807, 1998.
- [3.3] P.V.Nickles, V.N.Shlyptsev, M.Kalashnikov, M.Schnurer, I. Will, and W.Sandner, *Phys. Rev. Lett.*, vol. 78, pp. 2748-2751, 1997.
- [3.4] A. Rundquist, C.G. Durfee III, Z. Chang, C. Herne, S. Backus, M.M. Murnane, and H.C. Kapteyn, *Science*, vol. 280, pp. 1412-1415, 1998.
- [3.5] Yu.A.Uspenskii, S.V.Antonov; V.Yu.Fedotov, and A.V.Vinogradov, *Proc. SPIE*, vol. 3256, pp. 288–294, 1997.
- [3.6] Yu.A. Uspenskii, V.E. Levashov, A.V. Vinogradov, A.I. Fedorenko, V.V. Kondratenko, Yu.P.Pershin, E.N.Zubarev, and V.Yu.Fedotov, *Optics Letters*, vol. 23, no. 10 , pp. 771-773, 1998.
- [3.7] D. T. Attwood, P. Naulleau, K. A. Goldberg, E. Tejnil, C. Chang, R. Beguiristain, P. Batson, J. Bokor, E. M. Gullikson, M. Koike, H. Medecker, and J. H. Underwood, *IEEE J. Quant. Elect.*, vol. 35, no.5, pp. 709-720, 1999.
- [3.8] H.Zhang, A.Fohlisch, C.Kunz, A.Moewes, M.Pretorius, A.Ranck, H.Sievers, I.Storjohann, V.Wedemeier, and J.Voss, *Rev. Sci. Instr.*, vol. 66, no. 2, pp. 2021–2029, 1995.
- [3.9] U.Feldman, *Physica Scripta*, vol. 46, no. 3, pp. 202-220, 1992.
- [3.10] E.D. Palik, *Handbook of Optical Constants of Solids*. San Diego: Academic Press, 1998.
- [3.11] B.L.Henke, P.Lee, J.Tanaka, R.L.Simabukuro, and B.K.Fujikawa, *Atom. Data Nucl. Data Tables*, vol.27, pp.1–144, 1982.
- [3.12] H.R. Phillip, and H. Ehrenreich, *Phys. Rev.*, vol. 129, no. 4, pp. 1550-1560, 1963.
- [3.13] H.R. Phillip, *J. Appl. Phys.*, vol. 43, no. 6, pp. 2835-2839, 1972.
- [3.14] R.Soufli and E.Gullikson, *Appl.Opt.*, vol. 36, pp. 5499–5507, 1997

- [3.15] I.V.Kozhevnikov, V.E.Asadchikov, B.M.Alaudinov, A.Yu.Karabekov, and A.V.Vinogradov, *Proc. SPIE*, vol. 2453, pp. 141–153, 1995.
- [3.16] D.Y.Smith, “Dispersion Theory, Sum Rules, and Their Application to the Analysis of Optical Data,” in *Hanbook of Optical Constants of Solid*, Ed.E.D.Palik, Academic Press, Orlando, 1985, pp.35–64.
- [3.17] T.Takahagi, I.Nagai, A.Ishitani, H.Kuroda, and Y.Nagasawa, *J. App. Phys.*, v. 64, no. 7, pp.3515–3521, 1988.

## **CHAPTER 4**

### **GENERATION AND APPLICATION OF A HIGH AVERAGE POWER POLARIZED SOFT X-RAY LASER BEAM**

#### **4.1. Introduction**

The generation of intense polarized soft x-ray radiation is of significant interest for numerous applications. These include the diagnostics of materials surfaces and interfaces, the characterization of soft x-ray optical components, and the interaction of short wavelength radiation with atomic and molecular systems that involve anisotropy. Researchers have made extensive use of high average power beams of polarized coherent short wavelength radiation produced by undulators at modern synchrotron facilities [4.1]. Experiments have also been conducted with polarized soft x-ray radiation from laser produced plasmas [4.2]. The development of compact tabletop sources of high power polarized soft x-ray radiation can be expected to have a widespread impact applications in several fields.

Tabletop soft x-ray lasers, which are presently capable of generating coherent radiation with high peak and average power and high energy per pulse [4.3, 4.4], are excellent candidates for the generation of intense polarized short wavelength radiation. However, to date, the generation of polarized soft x-ray laser beams had been limited to experiments conducted at large laser facilities [4.5, 4.6, 4.7, 4.8, 4.9]. Typically soft x-ray

lasers that are based on the amplification of spontaneous emission in a plasma display a very low degree of polarization. The 19.6 nm laser line in a laser-pumped Ne-like Ge amplifier was observed to be polarized parallel to the target surface with a degree of polarization of 0.53 [4.5]. The polarization was accounted for by the anisotropy in the radiation trapping of the resonance line in an expanding plasma, which has a velocity gradient in the direction normal to the target surface. A larger degree of polarization in this line of Ne-like Ge was achieved by double-pass amplification using a half cavity in which an oblique incidence multilayer mirror was used as a polarizer [4.6]. A different approach in which the output of an injector plasma was linearly polarized and coupled into a Ne-like Ge amplifier produced polarized pulses of 23.2 and 23.6 nm radiation with a degree of polarization of  $\sim 0.98$  and a pulse energy of  $\sim 20$  nJ [4.7]. However, the average power in all these experiments was very low because the lasers were capable of firing at a maximum repetition rate of only several shots per hour.

The recent demonstration of high repetition rate discharge-pumped soft x-ray lasers discussed in [4.3, 4.10, 4.11] and chapter two, opens the opportunity of generating high average power polarized soft x-ray radiation with a tabletop device. As detailed in chapter 2, an average laser power of 3.5 mW and peak power of about 0.6 MW has been obtained utilizing a capillary discharge scheme. However, due to the high radial symmetry of the gain media generated using this scheme, the laser radiation can be expected to be essentially unpolarized. The recent development of high reflectivity multilayer mirrors at this wavelength makes possible the polarization of the beams produced by this compact tabletop source. This chapter details the generation of intense polarized 46.9 nm radiation using the combination of this tabletop discharge pumped Ne-

like Ar soft x-ray laser and a pair of Si/Sc mirrors designed to operate at an incidence angle of 45 degrees. The resulting polarized laser radiation was utilized to characterize the diffraction efficiency of a grating etched in single crystal silicon. This is to the knowledge of the author the first application of polarized soft x-ray laser radiation.

#### **4.2. Design and fabrication of the polarizing mirrors**

The polarizing mirrors for  $\lambda = 46.9$  nm were constructed based on high-reflectivity Sc/Si coatings [4.12], which has been recently successfully applied to soft x-ray laser beam manipulation and focusing [4.13, 4.14, 4.15]. To provide high polarization under reflection, the mirror reflectivity should be maximal for s-waves and minimal for p-waves. The structure of the multilayer mirrors was chosen to maximize the reflection of s-waves at an incidence angle of 45 degrees and a wavelength of 46.9 nm, and consisted of ten 44.5 nm thick periods with a thickness ratio of  $H(\text{Sc})/H(\text{Si})=0.43$ . The first layer deposited was a Si layer. A protective Si layer was deposited at the top of the stack. DC magnetron sputtering was used to achieve material deposition with a sufficiently low interface roughness of the order of 1.3 nm [4.12, 4.16]. The sputtering targets used consisted of 99.5 % pure Sc and a 4 inch diameter n-type Si wafer. The deposition rates for Sc and Si were held constant at 0.32 nm/s and 0.52 nm/s respectively. During all the deposition runs the gas used for sputtering was Ar, and the pressure in the reactor was kept at 0.43 Pa. The multilayer period and structure were analyzed by  $\text{CuK}\alpha$  and  $\text{CuK}\beta$  ( $\lambda=0.154$  nm and 0.179 nm) x-ray reflectometry.

The reflectivity for two polarizing multilayer mirrors was measured as a function of the angle of incidence. The experimental setup used to conduct the reflectometry

measurements as a function of angle was previously described [4.15]. In this set up the mirror is mounted on a computer-controlled rotation stage and illuminated with  $\sim 0.1$  mJ unpolarized laser pulses from a 46.9 nm Ne-like Ar capillary discharge soft x-ray laser operating at a repetition rate of 1 to 2 Hz. The reflected laser signal is measured for every shot and its intensity is normalized by a reference signal proportional to the intensity of the incoming beam. Figure 4.1 shows the measured reflectivity obtained as a function of angle for the two polarizers. The data shows that the reflectivity of each of the two polarizing mirrors reaches a local maximum of 22% and 25% at an angle of 45 degrees. At an incidence angle of 45 degrees the s-wave reflectivity is expected to be significantly higher than that of the p-wave reflectivity. Therefore the reflected beam will be partially linearly polarized.

### **4.3. Generation of a polarized soft x-ray laser beam**

The experimental setup that was used to polarize the laser beam is shown in figure 4.2. The vacuum chamber that housed the entire apparatus was placed at a distance of 1.5 m from the exit of the capillary discharge laser. The laser pulses were generated at a repetition rate of 1 Hz and were polarized by a Si/Sc multilayer-coated mirror fixed at an angle of 45 degrees respect to the incoming beam. To analyze the polarization of the beam a second multilayer-coated mirror, which maintained a 45 degree angle to the reflected beam, was rotated on the axis passing through the center of both mirrors. The laser was continuously fired at a repetition rate of 1 Hz while the analyzer mirror was rotated from 0 to 180 degrees. The intensity of the beam reflected by both mirrors was recorded using a vacuum photodiode that was mounted on a lever arm that followed the angular motion of the reflected beam. A 1 mm diameter pinhole was placed at the

entrance of the vacuum chamber in order to reduce the size of the beam to ensure that it could be completely captured by all of the optical components in the system. A 50% transmissive gold plated mesh was placed prior to the first mirror to split a portion of the incoming beam to a second fixed vacuum photodiode that monitored the intensity of the laser beam. This reference signal was used to normalize each data point to reduce the effect of the shot-to-shot fluctuations of the laser intensity. The photodiode signals corresponding to the reflected and reference beam intensities were recorded and stored for every laser shot using a 500 MHz analog bandwidth, 2 Gigasample/s digitizing oscilloscope (Hewlett-Packard model 54825A). Figure 4.3 shows the measured variation of the intensity of the laser beam after reflection on both mirrors as a function of the angle between the major axis of the polarization ellipse of the polarizer and the analyzer ( $\theta$  in figure 4.2, with  $\theta=0$  when the mirrors are parallel). Each data point was normalized by its corresponding reference intensity.

Due to the fact that the mirrors are not perfect polarizers, the determination of the degree of polarization requires theoretical analysis. The transformation of the beam by the pair of polarizers can be described using Stokes vectors or Mueller matrix formalism [4.17] as follows:

$$\begin{bmatrix} I^* \\ M^* \\ C^* \\ S^* \end{bmatrix} = \begin{bmatrix} \text{Si/Sc mirror} \\ \text{(analyzer)} \end{bmatrix} \begin{bmatrix} \text{Rotation about} \\ \text{propagation axis} \end{bmatrix} \begin{bmatrix} \text{Si/Sc mirror} \\ \text{(polarizer)} \end{bmatrix} \begin{bmatrix} I \\ M \\ C \\ S \end{bmatrix}$$

where  $I$  is the total beam intensity, and  $M$ ,  $C$  and  $S$  are the other three Stokes parameters that provide a complete description of the state of polarization of the beam. The intensity

of polarized light is given by,  $I_p^2 = M^{*2} + C^{*2} + S^{*2}$

Assuming that the polarizer and analyzer mirrors are identical (This assumption is justified by the reflectivity curves shown in figure 4.1),

$$\text{Si/Sc mirror} = \frac{1}{2} \begin{bmatrix} (R_s + R_p) & (R_s - R_p) & 0 & 0 \\ (R_s - R_p) & (R_s + R_p) & 0 & 0 \\ 0 & 0 & 2\sqrt{R_s R_p} \cos \Delta & -2\sqrt{R_s R_p} \sin \Delta \\ 0 & 0 & 2\sqrt{R_s R_p} \sin \Delta & 2\sqrt{R_s R_p} \cos \Delta \end{bmatrix}$$

Where  $R_{s,p}$  is the reflectivity for the s- and p-wave respectively, and  $\Delta$  is the phase shift between the s- and p-waves after reflection. The rotation matrix is given by:

$$\text{Rotation} = \begin{bmatrix} 1 & 0 & 0 & 0 \\ 0 & \cos 2\theta & \sin 2\theta & 0 \\ 0 & -\sin 2\theta & \cos 2\theta & 0 \\ 0 & 0 & 0 & 1 \end{bmatrix}$$

The angle  $\theta$  is the same as shown in figure 4.2 and represents the angle between the major axis of the polarization ellipse for the polarizer and analyzer mirrors. The initial Stokes vector in this case describes unpolarized light with a normalized intensity and has the following values:  $I=1$ ,  $M=0$ ,  $C=0$  and  $S=0$ . After matrix manipulation, the final Stokes vector describing the beam exiting the second mirror is found to be:

$$\begin{bmatrix} I^* \\ M^* \\ C^* \\ S^* \end{bmatrix} = \frac{1}{2} \begin{bmatrix} (R_s^2 + R_p^2) \cos^2 \theta + 2R_s R_p \sin^2 \theta \\ (R_s^2 - R_p^2) \cos^2 \theta \\ -\sqrt{R_s R_p} (R_s - R_p) \sin 2\theta \cos \Delta \\ -\sqrt{R_s R_p} (R_s - R_p) \sin 2\theta \sin \Delta \end{bmatrix}$$

The degree of polarization is,

$$p = \frac{I_p}{I^*} = \frac{\sqrt{[(R_s^2 - R_p^2) \cos^2 \theta]^2 + [-\sqrt{R_s R_p} (R_s - R_p) \sin 2\theta]^2}}{(R_s^2 + R_p^2) \cos^2 \theta + 2R_s R_p \sin^2 \theta}$$

Fitting the expression for  $I^*$  to the measured intensity distribution in figure 4.3 it is possible to obtain the normalized values for  $R_s$  and  $R_p$ . In order to obtain  $R_s$  and  $R_p$  it is necessary to include the measured reflectivity of the non-polarized beam at an incidence angle of 45 degrees where  $R(45) = \frac{1}{2} (R_s + R_p)$ . Using an average value of  $R(45) = 23.5\%$  obtained from the measurements (see figure 4.1),  $R_s$  and  $R_p$  are determined to be 0.414 and 0.056 respectively. Using these values, the maximum degree of polarization, which occurs at angles  $\theta = 0$  and 180 degrees is  $p = 0.965$ . This value, obtained assuming identical polarizing mirrors, represents the lower limit of the degree of polarization achieved. Considering that in reality the mirrors are similar but not identical, the maximum degree of polarization obtained is slightly higher. The remaining parameters of a polarized beam (type of polarization and direction) can also be determined by the Stokes parameters. The angle of the major axis of the polarization ellipse respect to the s direction of the second mirror is,

$$\zeta = \frac{1}{2} \tan^{-1} \left( \frac{C^*}{M^*} \right)$$

and the ratio of the major to minor axis is,

$$\eta = \frac{I^*}{|S^*|} + \sqrt{\left( \frac{I^*}{|S^*|} \right)^2 - 1}$$

Although it is not possible to determine  $\Delta$  in  $C^*$  and  $M^*$  and thus  $\zeta$  and  $\eta$  for all angles  $\theta$  using the experimental setup reported herein, at  $\theta = 0$  and  $180$  degrees  $S^* = 0$  and  $C^* = 0$ . Therefore, at  $\theta = 0$  the beam is linearly polarized with 96.5% degree of polarization and aligned in the s direction of the second mirror. The overall efficiency for the two mirror polarization system at  $\theta = 0$  and  $180$  degrees is  $I^*/I = 0.5(R_s^2 + R_p^2) = 8.7\%$ . When the laser that was used in this work is optimally configured, it is possible to extract up to  $\sim 0.88$  mJ per pulse and an average power of 3.5 mW operating at 4 Hz [10]. Therefore given the efficiency of the polarizer system described herein it should be possible to generate a  $\sim 0.3$  mW average power (76  $\mu$ J/pulse average at 4 Hz) soft x-ray laser beam that is better than 96% polarized. The next section discusses the use of this polarized beam in the characterization of the efficiency of a diffraction grating.

#### 4.4. Characterization of diffraction gratings

The experimental set up utilized to characterize the diffraction efficiency of gratings for polarized 46.9 nm radiation is illustrated in figure 4.4. The measurements were conducted in the same vacuum chamber used in the polarization experiment described in the previous section. As in the previous case a 1mm-diameter pinhole was placed at the entrance of the vacuum chamber to reduce the spot size of the laser beam

incident on the grating with the purpose of measuring the diffraction efficiency at large angles of incidence. To facilitate these measurements the grating was mounted on a rotational stage. The 46.9 nm laser radiation produced by the capillary discharge pumped Ne-like Ar laser was polarized utilizing the set of two 45 degrees Si/Sc multilayer mirrors described in the previous sections. The intensity of the beams corresponding to each of the different diffracted orders was measured with a vacuum photodiode (labeled “A” in figure 4.4) that was mounted on a rotating arm driven by a stepper motor. The data was also normalized for each pulse by the intensity of the incident laser beam for each pulse, monitored by a fixed vacuum photodiode, identified by “B” in figure 4.4. The intensity of the radiation for each of the diffraction orders was determined by operating the laser at a repetition rate of 1 Hz and averaging 30 consecutive laser shots. To obtain absolute measurements of the diffraction efficiency, the vacuum photodiode “B” was placed between the second polarizer and the grating, and the ratio of the intensities between this signal and that of the reference photodiode was used for normalization. The diffraction efficiency for unpolarized radiation was also measured. In this case the polarizers were removed from the set up and the radiation emitted by the laser was directed to impinge directly onto the grating.

The diffraction grating that was characterized in this experiment was prepared by ion beam etching of single crystal silicon. It had a rectangular groove profile with a line density of 1200 lines per millimeter. The width of the grooves corresponded to 77% of the period, and their depth was 17.6 nm. Figures 4.5a and 4.5b show the measured diffraction efficiency for p- polarization and unpolarized radiation respectively for incidence angles of 60, 70 and 80 degrees. Measurements were conducted for all the

diffraction orders present at each of the incidence angles. The results shown are the average of at least 5 sets of measurements each containing 30 laser shots for each of the diffraction orders. The error in the overall measurement was estimated to range from less than 1 percent in the case of the zero order at 80 degrees grazing angle of incidence for which the signal is large, to 30 percent for the second order signals that have a very low intensity (often less than 1 percent of the impinging radiation). The diffraction efficiency at 46.9 nm is observed to be poor, reflecting the fact that the grating was designed for optimum operation in the range of 5-10 nm. The intensity of the zero order dominates for all angles and increases as a function of the grazing incidence angle, as a consequence of the increase of the reflectivity of the material with the angle of incidence. As expected, the first order diffraction efficiency is larger for unpolarized radiation than for p-polarized radiation. The first order and minus one order present maximum efficiency of nearly 3.5 percent at 60 and 70 degrees incidence angle respectively.

#### **4.5. Conclusion**

In summary, a technique for the generation of high average power polarized soft x-ray laser beams has been demonstrated utilizing a compact tabletop set up. A pair of Si/Sc multilayer mirrors designed for operation at 45 degrees was used to polarize the output of a high repetition rate tabletop 46.9 nm laser to a degree of polarization exceeding 96 percent. The resulting polarized beam was used to characterize the diffraction efficiency of a diffraction grating etched on a Si substrate. This is to the author's knowledge the first report of the use of a polarized soft x-ray laser beam in an application. This intense polarized soft x-ray laser can be expected to find important use in ellipsometry at short wavelengths and other applications.

#### 4.6. Figures

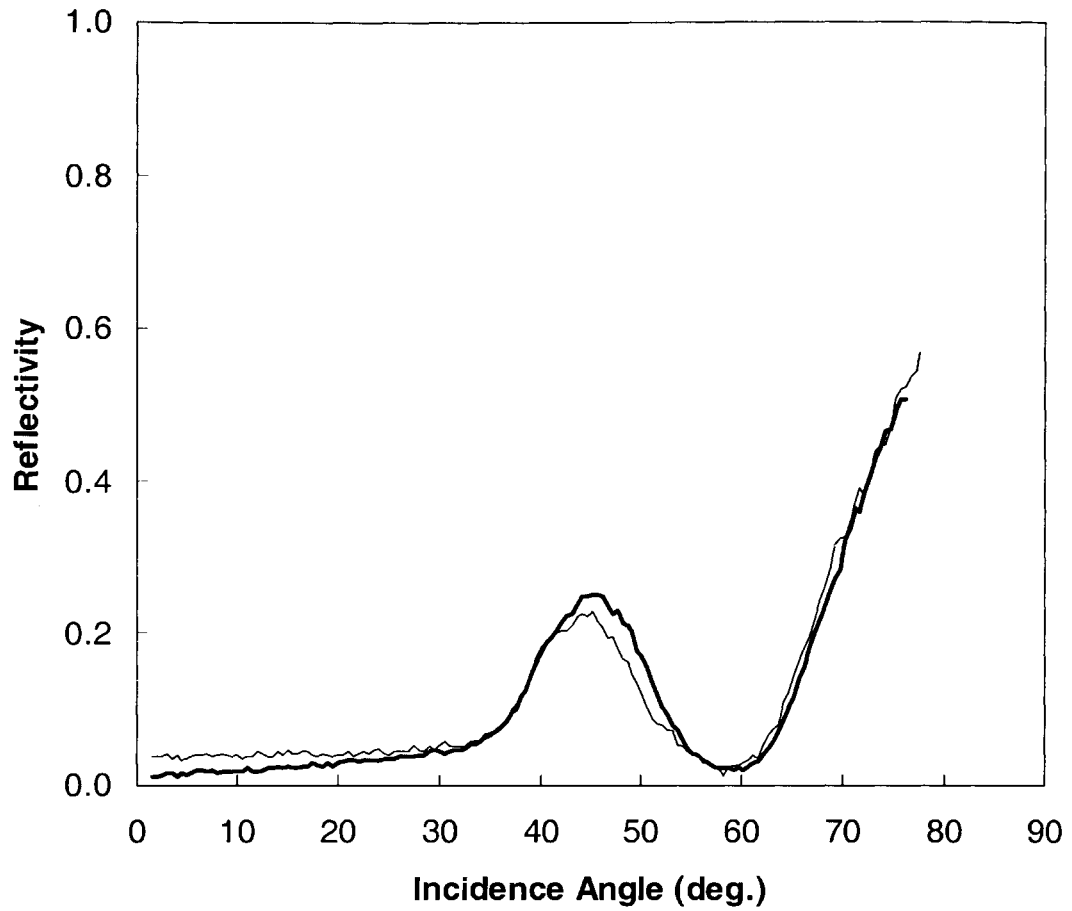


Figure 4.1. Measured reflectivity of the Si/Sc multilayer mirrors at 46.9nm as a function of angle of incidence.

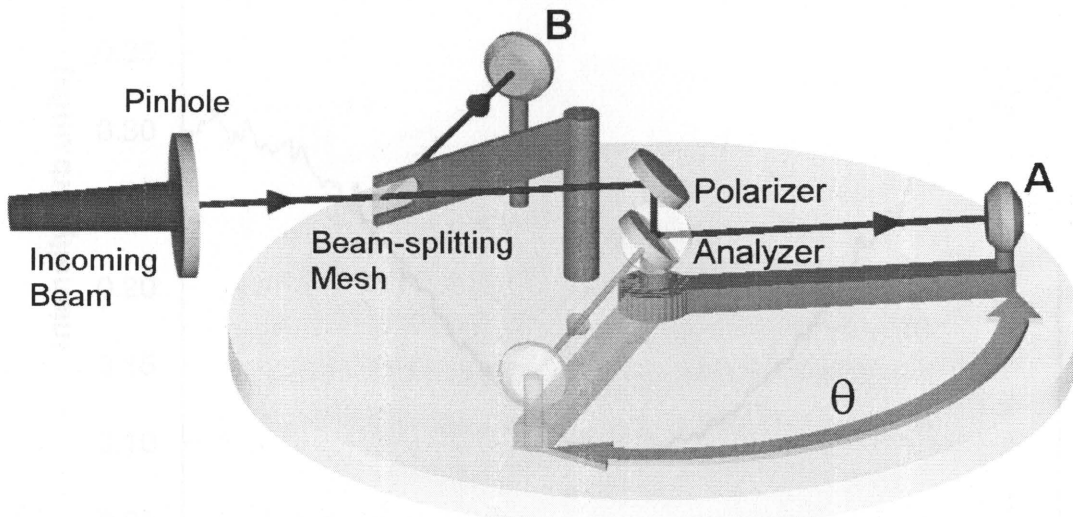


Figure 4.2. Schematic representation of the setup utilized to polarize the laser beam. Labels A and B identify the fixed and rotating vacuum photodiodes respectively.

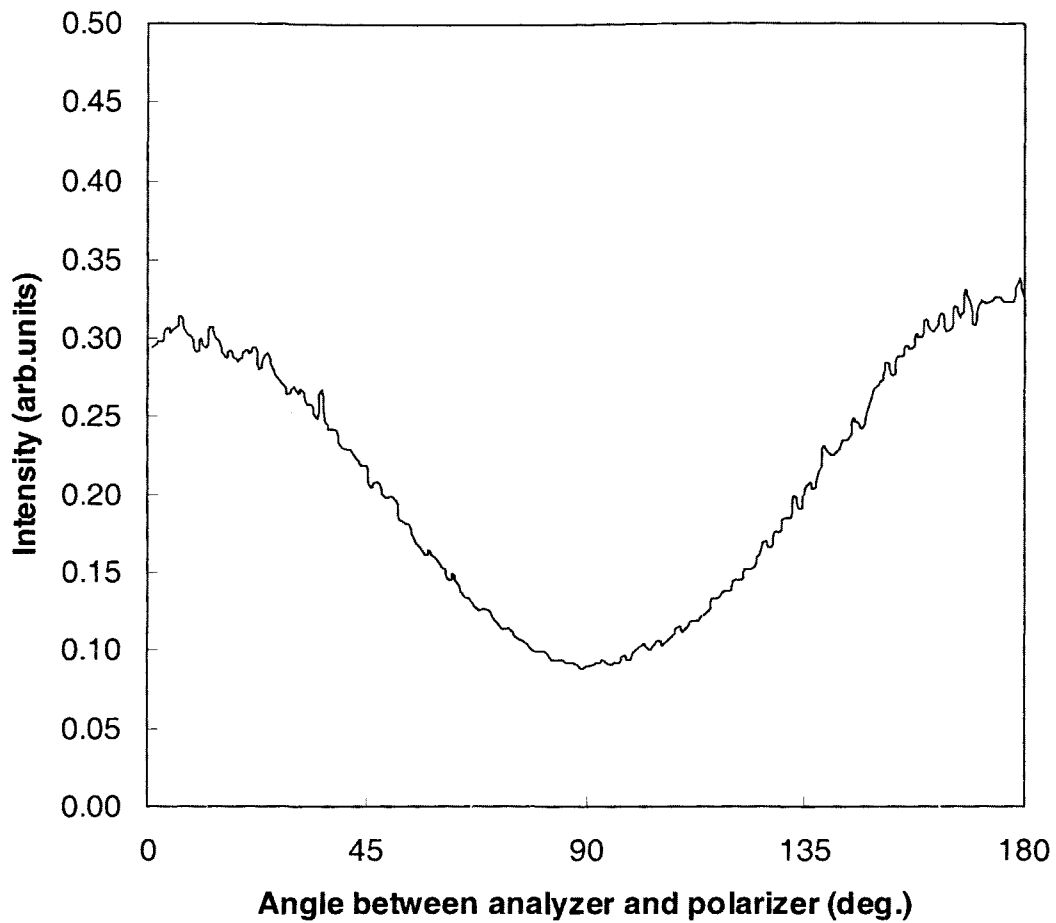


Figure 4.3. Intensity of the beam after passing through the pair of polarizers as a function of the angle  $\theta$  between them.

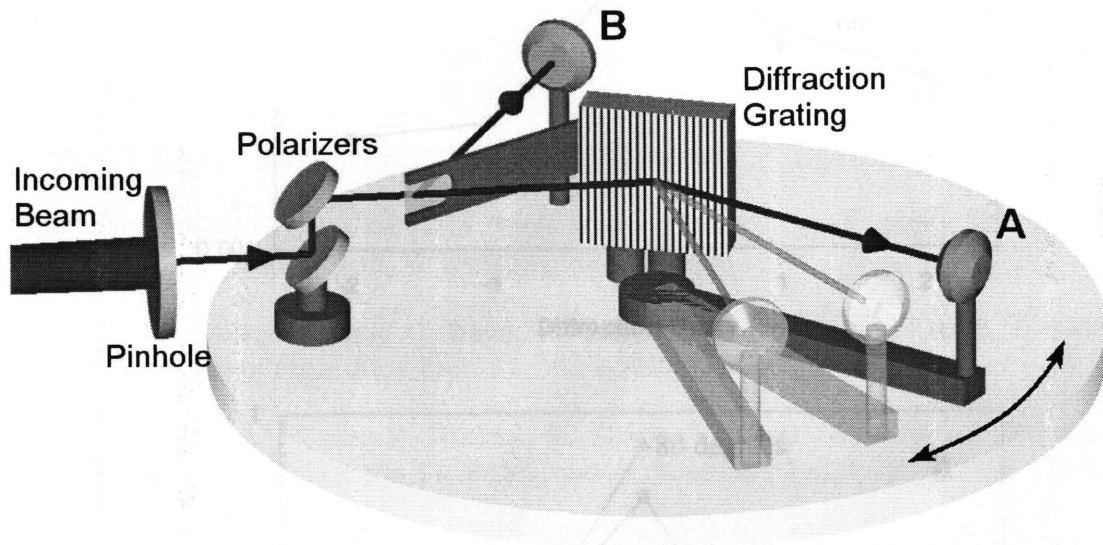


Figure 4.4. Schematic representation of the experimental set up used to characterize the diffraction efficiency of a grating.

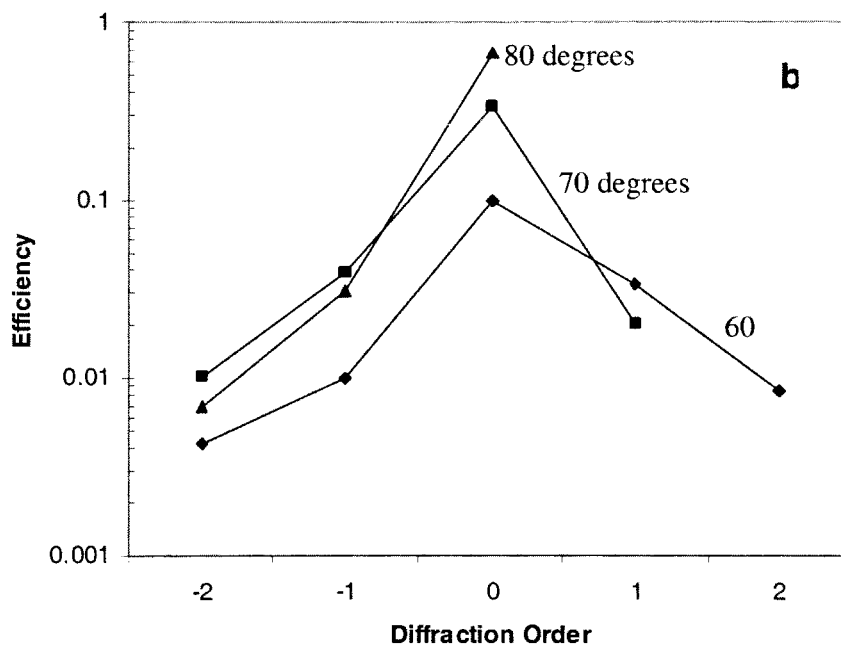
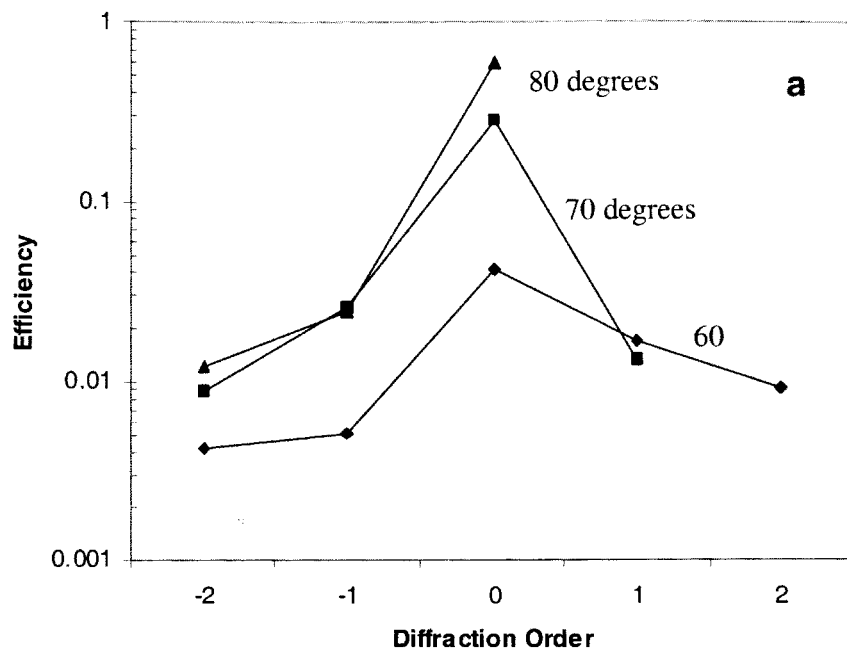


Figure 4.5. a) Diffraction efficiency of the different orders for p-polarized radiation at three different angles of incidence. b) Diffraction efficiency for unpolarized radiation.

#### 4.7. References

- [4.1] D.T. Attwood, P. Naulleau, K. A. Goldgerg, E. Tejnil, C. Chang, R. Beguiristain, P. Batson, J. Bokor, E. Gullikson, M. Koibe, H. Medecky and J.H. Underwood, *IEEE J. Quant. Elect.* 35, 709-720, (1999).
- [4.2] M. Yamamoto, K. Mayama, H. Nomura, H. Kimura, M. Yanagihara, and T. Namioka, *SPIE Proc.*, 1720, pp.390-394, 1992.
- [4.3] J.J. Rocca , *Rev. Sci. Inst.* 70, 3799-3827, (1999).
- [4.4] For example see articles in “Soft x-ray lasers and applications III”, *SPIE Vol 3776*, J.J. Rocca and L.B. Da Silva, Eds. , (1999).
- [4.5] T. Kawachi, K. Murai, G. Yuan, S. Ninomiya, R. Kodama, H. Daido, Y. Kato and T. Fujimoto, *Phys. Rev. Lett.* 75, 3826-3929, (1995).
- [4.6] K. Murai, G. Yuan, R. Kodma, H. Daido, Y. Kato, M. Niibe, A. Miyake, M. Tsukamoto, Y. Fukuda, D. Neely, and A. MacPhee. *Jpn. J. Appl. Phys.* 33, L600-L603 (1994).
- [4.7] B. Rus, C.L.S. Lewis, G. F. Cairns, P. Dhez, P. Jaegle, M.H. Key, D. Neely, A.G. MacPhee, S.A. Ramsden, C.G. Smith and A. Sureau, *Phys. Rev. A.* 51, 2316-2327, (1995).
- [4.8] Sureau and P.B. Holden, *Phys. Rev. A* 52, 3110-3125, (1995).
- [4.9] D. Benredjem, A. Sureau, and C. Moller, *Phys. Rev. A.* 56, 4576-4584, (1997).
- [4.10] C.D. Macchietto, B.R. Benware and J.J. Rocca, *Optics Lett.* 24, 1115-1117, (1999).
- [4.11] B.R. Benware, C.D. Macchietto, C.H. Moreno, and J.J. Rocca, *Phys. Rev. Lett.* 81, 5804-5807 (1998).
- [4.12] Yu. A. Uspenskii, V.E. Lebashov, A.V. Vinogradov, A.I. Fedorenko, V.V. Kondratenko, Yu. P. Pershing, E.N. Zubalev, and V. Yu Fedotov, *Optics Lett.* 23, 771-773, (1998).
- [4.13] B.R. Benware, A. Ozols, J.J. Rocca, I.A. Artiukov, V.V. Kondratenko and A.V. Vinogradov, *Optics Lett.* 24, 1714-1716, (1999).

- [4.14] J.J. Rocca, C.H. Moreno, M.C. Marconi, and K. Kanizay, *Optics Lett.* 24, 420-422, (1999); and C.H. Moreno, M.C. Marconi, K. Kanizay, J.J. Rocca, Yu.A. Uspenskii, A.V. Vinogradov, Yu.P. Pershin, *Phys. Rev. E* 60, 911-917 (1999).
- [4.15] I.A. Artioukov, B.R. Benware, J.J. Rocca, M. Forsythe, Yu. A. Uspenskii and A.V. Vinogradov, *IEEE J. Sel. Top. Quant. Elect.* 5, 1495-1501 (1999).
- [4.16] V.E. Levashov, Yu.A. Uspenskii, A.V. Vinogradov, A.I. Fedorenko, V.V. Kondratenko, Yu.P. Pershin, E.N. Zubarev, S. Mrowka and F. Schaeffer, *Int. Phys. Conf. Ser. N 159*, 593, IOP Publisher Ltd. (1999).
- [4.17] D. Clarke and J.F. Granger, "Polarized light in optical measurements". Pergamon Press, Elmsford, NY (1971).

## CHAPTER 5

# FOCUSING OF A TABLETOP SOFT X-RAY LASER BEAM AND LASER ABLATION

### 5.1. Introduction

Soft x-ray lasers have been shown to have sufficient intensity to produce high resolution images in a single shot [5.1, 5.2]. Recent advances in table-top sources of soft x-ray coherent radiation create the possibility to generate short wavelength radiation pulses of unprecedented high peak intensities at high repetition rates [5.3]. Focusing of these intense beams will open new applications, including non-linear optics at ultrashort wavelengths, nanomachining, and the generation of plasmas with soft x-ray photons. High order harmonic pulses with a wavelength near 55 nm and subpicosecond duration have been recently focused to reach an estimated intensity of  $1 \times 10^{11}$  W/cm<sup>2</sup> [5.4]. Focusing of table-top soft x-ray lasers which are now capable of producing millijoule-level pulses [5.5] should also yield very high intensities while allowing for much higher energy density. Recently, nanojoule pulses from the 15.47nm line of Li-like Al were focused into a sub-micrometer spot to obtain an intensity of  $\approx 2 \times 10^7$  W/cm<sup>2</sup> [5.6]. Preliminary results of an attempt to focus laser pulses of much higher energy from a collisional soft x-ray laser pumped by a large optical laser have been also reported [5.7]. In this letter we report the generation and characterization of a focused soft x-ray laser

beam with intensity and energy density that significantly exceed the threshold for the ablation of metals. The results were obtained by focusing 0.13 mJ laser pulses of 1.2 ns FWHM duration produced by the table-top capillary discharge Ne-like Ar laser ( $\lambda=46.9\text{nm}$ ) described in chapter 2 with a spherical Si/Sc multilayer mirror.

## 5.2. Experimental setup

The experimental set-up is shown in figure 5.1. The laser pulses were generated at a repetition rate of 1 Hz by amplification in a 18.2 cm long Ar capillary plasma excited with a fast current pulse [5.8]. The far field laser beam profile had an annular shape and a peak to peak divergence of about 4.6mrad [5.8]. The laser intensity distribution near the exit of the amplifier was verified to be also annular; the unfocused laser beam ablated a ring pattern with a peak to peak diameter of  $\approx 340\ \mu\text{m}$  onto a piece of acrylic placed at 1.1 cm from the end of the capillary. The annular intensity distribution is caused by refraction of the rays in the amplifier due to radial density gradients [5.9, 5.10]. The laser beam was focused with a spherical ( $R=10\ \text{cm}$ ) Si/Sc multilayer-coated mirror positioned in a vacuum chamber at 256.5 cm from the exit of the capillary discharge amplifier. The multilayer coating was deposited using magnetron sputtering [5.11] on a 2.5 cm diameter superpolished borosilicate substrate having an RMS surface roughness of 0.1 nm. The normal incidence reflectivity of these multilayer coatings was measured to be  $\approx 43\%$  at 46.9 nm. The mirror was positioned at normal incidence with the purpose of minimizing aberrations, and the reflected beam was focused onto the narrowest side of a thin metal strip (1.6 mm thick,  $\approx 1\text{cm}$  wide). The measurements reported herein employed a brass target, but similar results were obtained using stainless steel. It can be noticed that in this

set up the target also intercepts part of the incoming beam. However, this is not problematic because the target blocks only a small fraction of the incoming beam, which at that location has a diameter of about 12 mm. The focused laser beam was observed to readily ablate metals within several hundred  $\mu\text{m}$  from the focus, creating a visible plasma plume. The imprints on the metal surface give useful two-dimensional information of the focused laser beam intensity distribution, in spite of the dependence of the size of the molten region on the heat conductivity, melting point of the sample material, and duration of the laser pulse [5.12]. To monitor the focused beam intensity distribution at different planes along the propagation axis we mounted the target on a translation stage driven by a computer controlled stepper motor. The axis of motion of the translation stage was positioned at an angle of 50 degrees respect to the optical axis. Series of imprints of the beam profile along the optical axis were obtained by continuously moving the translation stage while repetitively firing the laser at 1Hz.

### **5.3. Results**

Figure 5.2 is a scanning electron microscope (SEM) photograph showing the progression of ablation patterns obtained as the target was moved away from the mirror towards the focus. It shows the convergence of the beam within an axial region of about 450  $\mu\text{m}$  near the focus. The sampling distance between any two contiguous shots is 22.2  $\mu\text{m}$  along the optical axis (notice that this axial distance between patterns is smaller than it appears in the SEM photographs because the sample is moved at an angle with respect to the optical axis). Each ablation pattern is the result of a single laser shot. Figure 5.3 shows part of the same sequence with larger magnification. At a distance of a few

hundred  $\mu\text{m}$  from the focal region the ablated patterns have the shape of thin annular disks. The patterns have good azimuthal symmetry, except for a small discontinuity where the incoming beam was blocked by the target. As the focal region is approached the thickness of the ablated rings is observed to increase and an ablated spot develops at the center. The depth of these annular grooves was measured to be  $\approx 2 \mu\text{m}$  using a visible laser interferometer. Finally, very near the focus the patterns evolve into a single spot with a deep hole on axis. The smallest ablated spot has a diameter of about  $17 \mu\text{m}$ , and contains a deep hole of  $\approx 3 \mu\text{m}$  diameter on axis. Not shown in figure 5.3 are the ablation patterns obtained positioning the target on the other side of the focus at increasing distances from the mirror, which rapidly become diffused and more difficult to distinguish.

#### **5.4. Ray tracing computations**

Ray tracing computations were conducted to analyze the results and obtain an estimate of the power density achieved. The beam was approximated assuming a point source located at 263cm from the mirror with an angular distribution tailored to closely match the measured laser beam intensity in the near-field and far-field. Similar results were obtained simulating the source with a  $300 \mu\text{m}$  diameter disk. The trajectory of  $1.3 \times 10^4$  rays was computed to simulate the beam propagation. Figure 5.4 shows the computed cross section of the beam intensity distributions in the focal region. For comparison with the experiment the measured boundaries of the ablated regions are represented with black dots in the same figure. All the major features of the observed ablation profiles of figures 5.2 and 5.3 are well described by the ray tracing

computations. The computations show that a few hundred  $\mu\text{m}$  away from the focal region the highest concentration of rays defines thin annular disks. Also in accordance with the experiment a high intensity peak is observed at the axis as the focal region is approached. Both features are the result of the spherical aberration that causes the rays to converge and cross at these locations. Therefore, the observed annular ablation patterns are not a direct consequence of the annular profile of the laser beam. The spherical aberration would also cause similar rings for any beam profile with a sufficient intensity in the periphery (such as a flat intensity distribution). Likewise, the spherical aberration causes the central peak, which begins to develop when the outer-most rays converge on axis. Near the so-called “plane of minimum confusion” the intensity distribution is computed to be dominated by the sharp central peak, which causes the deep holes observed at the center of the ablation patterns shown near the bottom of figure 5.3. The average intensity within a 2  $\mu\text{m}$  diameter central region is estimated to be  $\approx 1 \times 10^{11}$   $\text{W}/\text{cm}^2$  from the computed fraction of rays that intersect this region. The corresponding energy density within this central region is  $\approx 100 \text{ J}/\text{cm}^2$ . The analysis also confirms that the minimum spot size is dominantly determined by the spherical aberration, and not by the partial spatial coherence of the laser beam [5.13].

## 5.5. Conclusion

In summary, a spherical multilayer mirror was used to focus high energy laser pulses (0.13 mJ) generated by a 46.9 nm table-top capillary discharge amplifier, realizing the first clear demonstration of material ablation with a coherent soft x-ray beam. The peak intensities obtained are estimated to be  $\approx 1 \times 10^{11}$   $\text{W}/\text{cm}^2$ , dominated by the spherical

aberration. Considering that Ne-like Ar laser pulses with energy near 1 mJ have been recently generated at 4 Hz repetition rate [5.5], intensities of the order of  $1 \text{ TW/cm}^2$  should be readily obtained with the same focusing set up, opening new applications for table-top soft x-ray lasers. The use of specially shaped focusing optics should allow for significantly higher intensities.

## 5.6. Figures

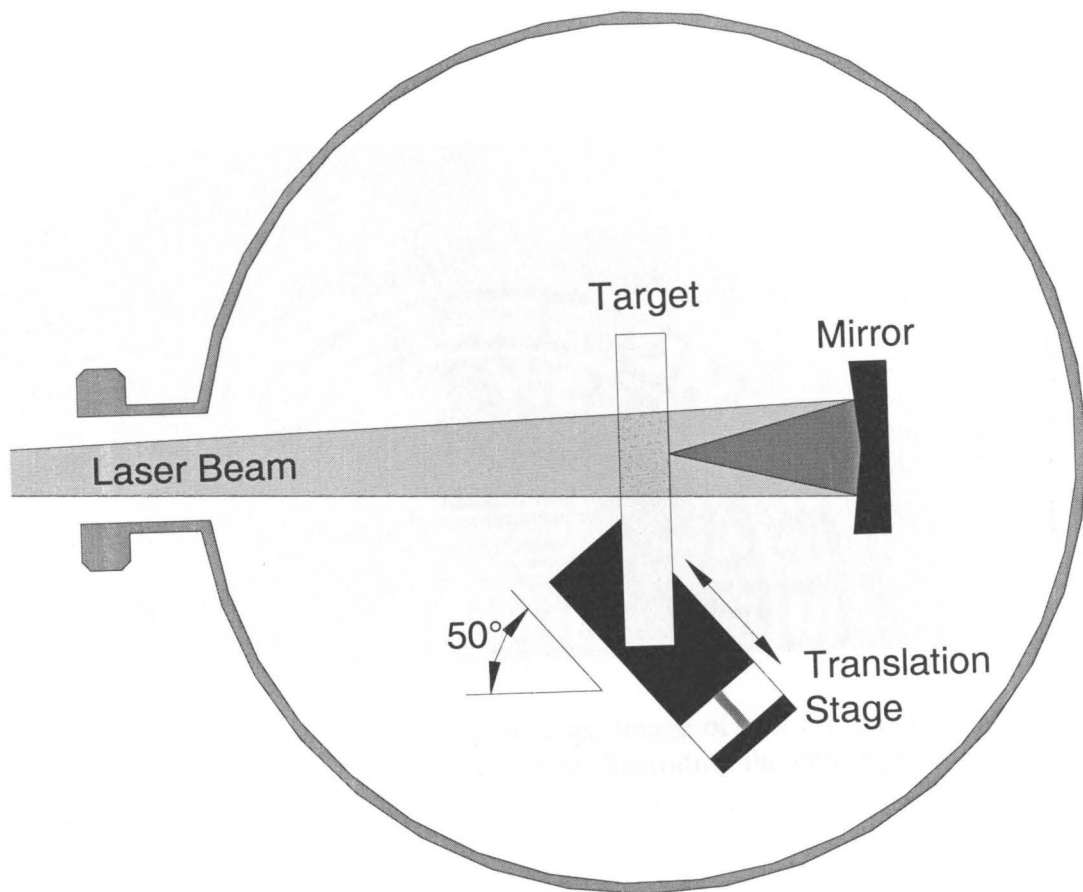


Figure 5.1. Experimental set up used to focus and characterize the soft x-ray laser beam.

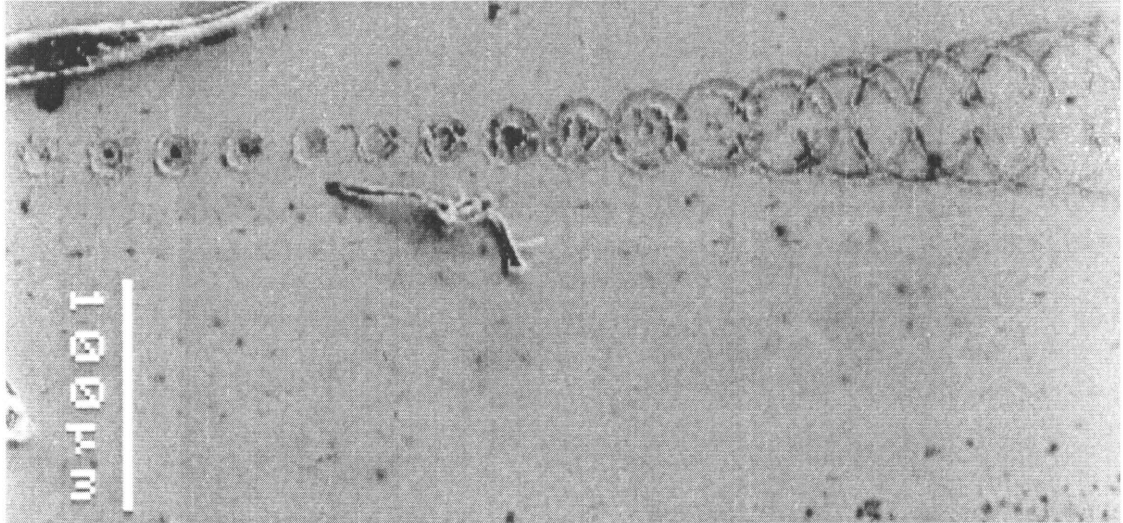


Figure 5.2. Scanning electron microscope image of soft x-ray laser ablation patterns on the surface of a brass sample illustrating the convergence of the focused beam.

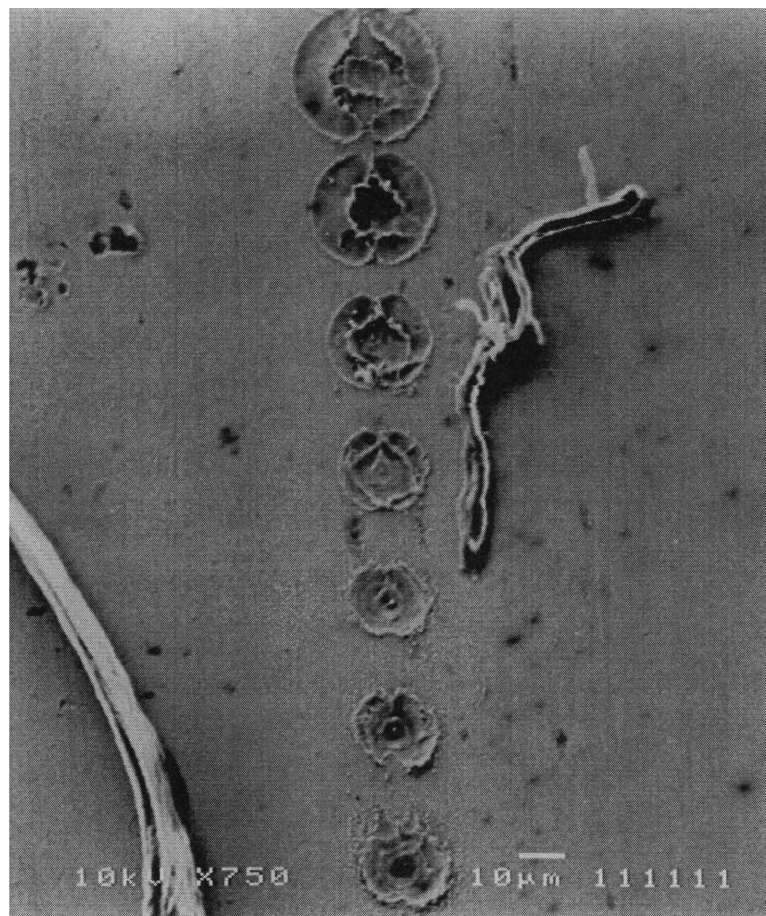
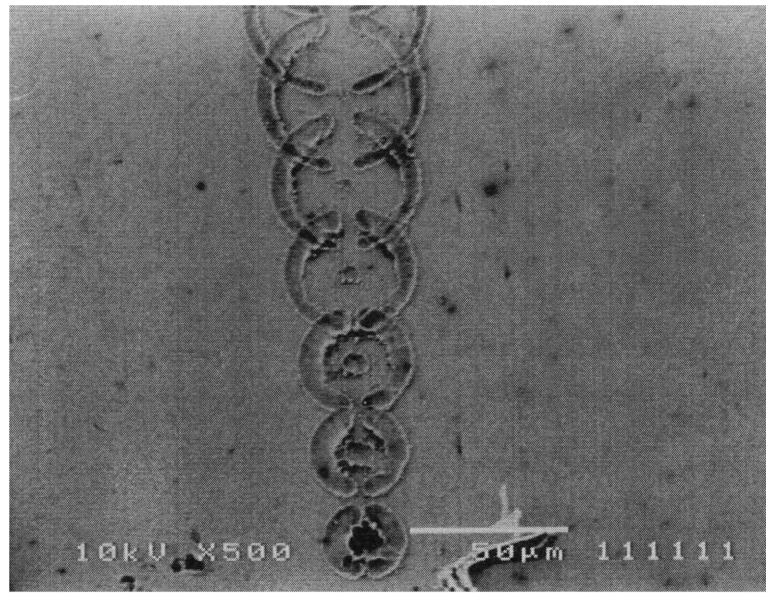


Figure 5.3. Scanning electron microscope images of the ablation patterns in the focal region.

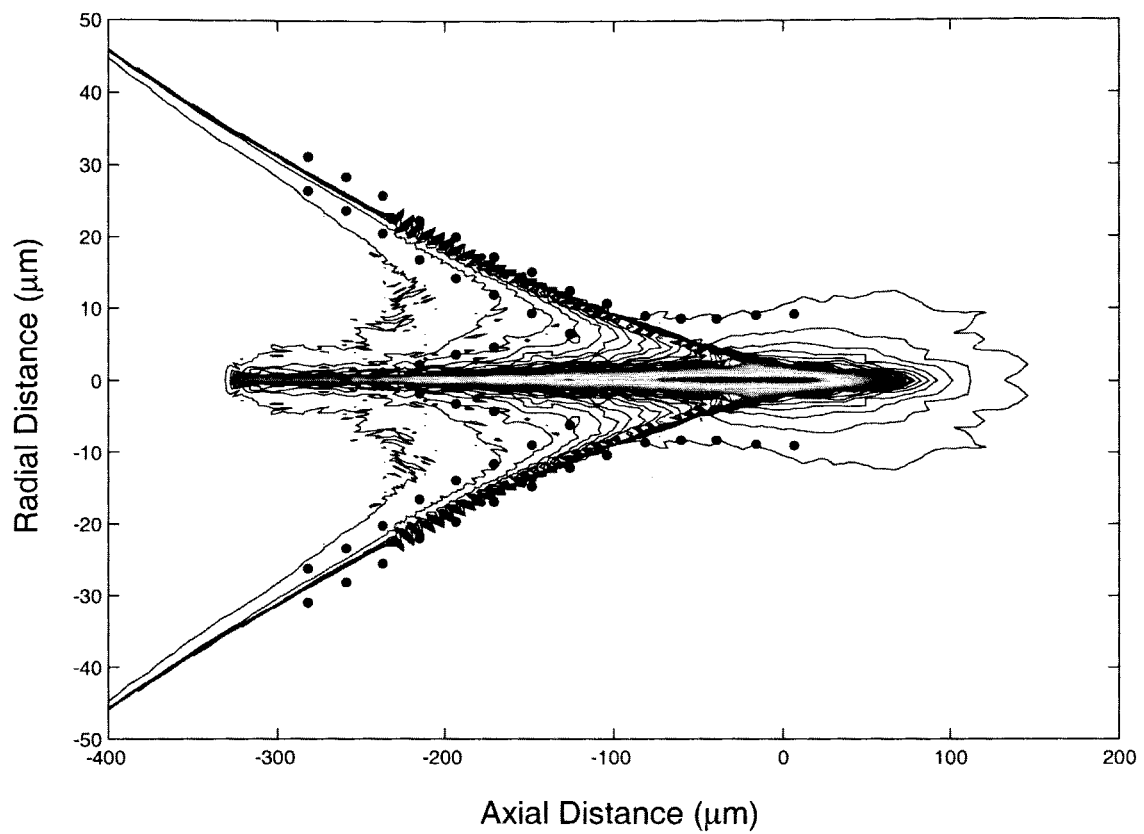


Figure 5.4. Computed cross section of the beam in the focal region. The dots are the measured boundaries of the patterns ablated on a brass sample.

## 5.7. References

- [5.1] D.S. Di Cicco, D. Kim, R. Rosser and S. Suckewer. *Opt. Lett.*, **17**, 157, (1992).
- [5.2] L.B. Da Silva, J.E. Trebes, R. Balhorn, S. Mrowka, E. Anderson, D.T. Atwood, T.W. Barbee Jr. , J. Brase, M. Corzett, J. Gray, J.A. Koch, C. Lee, D. Kern, R.A. London, B.J. McGowan, D.L. Matthews, G. Stone, *Science*, **258**, 269 (1992).
- [5.3] See papers in “Soft X-Ray Lasers and Applications III”. Eds. J.J. Rocca and L.B. Da Silva. SPIE vol 3776, (1999).
- [5.4] L. Le De’roff, P. Salie’res and B. Carre’, *Opt. Lett.* **23**, 1544, (1998).
- [5.5] C.D. Macchietto, B.R. Benware and J.J. Rocca, *Opt. Lett.*, **24**, 1115, (1999).
- [5.6] T. Ohchi, N. Yamaguchi, C. Fujikawa and T. Hara, pp. 683, “X-Ray Lasers” 1998, eds. Y. Kato, H. Takuma and H. Daido, IOP Conf. Proc. No 159, (1999).
- [5.7] P. Zeitourn, S. Sebban, K. Murai, H. Tang et al. p 677 ,“X-Ray Lasers”, 1998, eds. Y. Kato, H. Takuma and H. Daido, IOP. Conf. Proc. No 159, (1999).
- [5.8] B.R. Benware, C.D. Macchietto, C.H. Moreno and J.J. Rocca, *Phys. Rev. Lett.*, **81**, 5804 (1998).
- [5.9] C.H. Moreno, M.C. Marconi, V.N. Shlyaptsev, B.R. Benware, C.D. Macchietto, J.L.A. Chilla, J.J. Rocca, and A.L. Osterheld, *Phys. Rev. A* **58**, 1509 (1998).
- [5.10] J.L.A. Chilla and J.J. Rocca. *J. Opt. Soc. Am.* **B13**, 2841, (1996).
- [5.11] Yu. A. Uspenskii, V. E. Lebashov, A. V. Vinogradov, A. I. Fedorenko, V.V. Kondratenko, Yu. P. Pershin, E.N. Zubalev and V. Yu. Fedotov, *Opt. Lett.* **23**, 771, (1998).
- [5.12] J.C. Miller and R.F. Haglund, “Laser ablation and desorption”, Academic Press. San Diego, (1998).
- [5.13] M.C. Marconi, J.L.A.Chilla, C.H. Moreno, B.R. Benware and J.J. Rocca, *Phys. Rev. Lett.* **79**, 2799, (1997).

## CHAPTER 6

### SUMMARY

In conclusion, a new generation capillary discharge table-top laser operating at 46.9 nm that makes use of ceramic capillaries and longer plasma column lengths has been developed and characterized. Average powers of up to 3.5 mW at a repetition rate of 4 Hz and average pulse energies of 0.88 mJ have been demonstrated. A lower average power of ~1mW at a higher repetition rate of 7 Hz has also been observed. Even higher repetition rates of up to 10Hz at diminished output powers have also been noted. The temporal evolution of the laser pulse has been measured to be 1.2 ns-1.5 ns with peak instantaneous powers reaching >500 kW. Far field beam profile measurements show that the beam exhibits an annular profile with a peak to peak divergence of 4.6 mrad that is the result of refraction of the rays due to the steep density gradients that exist in the plasma.

This laser that is of a size that is comparable to many widely utilized commercially available visible and UV lasers has also been demonstrated to be a practical source of coherent soft x-ray radiation by performing a series of experiments using the beam. In all of these experiments, this laser was advantageous to the application by not only providing a high brightness source, but also being able to deliver the beam at repetition rates that are typical in a laboratory environment.

Angular dependent reflectivity has been performed to determine optical constants of materials at a wavelength of 46.9 nm, which are in good agreement with those previously measured, or in some cases represent the first recorded values for those materials. A technique was developed to accurately extract the optical constants regardless of the presence of a surface layer, which at this wavelength has a large impact on the reflectivity of the material. This experiment represents the first application of a table-top soft x-ray laser to the field of material characterization.

Many applications in the future will require a polarized beam in addition to the qualities mentioned above. To this end, an optical system comprised of two multi-layer coated mirrors was used to polarize the output beam of the laser developed in this work. The two mirrors were specially designed for an optimum reflectivity at an incidence angle of 45 degrees and wavelength of 46.9 nm. Due to the partial polarizing effect of the mirrors, a method was developed to determine the degree polarization using a Mueller's matrix formalism. The maximum degree of polarization was determined to be 0.965 with an efficiency of the polarizing system of 8.7%. The polarized beam was used to characterize the efficiency of a diffraction grating etched on a Si substrate.

In the last experiment of this work, the focal region of the output beam that was focused using a spherical multi-layer coated mirror was characterized. Due to the high instantaneous power of the laser, it was possible to directly imprint ablation patterns on brass targets in the focal region. Ray tracing computations that are in excellent agreement with the observed physical characteristics of the ablation patterns were used to determine an estimated peak intensity of  $1 \times 10^{11}$  W/cm<sup>2</sup>. The ray tracing computations also show that the majority of the energy is contained within a 2  $\mu$ m diameter spot near

the plane of minimum confusion and that this spot size is limited by spherical aberration of the mirror.